Thesis for the degree of Doctor of Philosophy

Magnetic fields around massive protostars as traced by masers and dust emission

DARIA DALL'OLIO

CHALMERS

Astronomy and Plasma Physics
Department of Space, Earth and Environment
CHALMERS UNIVERSITY OF TECHNOLOGY
Gothenburg, Sweden 2020

Magnetic fields around massive protostars as traced by masers and dust emission
DARIA DALL'OLIO

ISBN:978-91-7905-365-9
Doktorsavhandlingar vid Chalmers tekniska högskola
Ny serie Nr 4832
ISSN 0346-718X

Division of Astronomy & Plasma Physics
Department of Space, Earth and Environment
Chalmers University of Technology
SE–412 96 Gothenburg, Sweden
Phone: +46 (0)31–772 1000

Contact information:
Daria Dall'Olio
Onsala Space Observatory
Chalmers University of Technology
SE–439 92 Onsala, Sweden

Phone: +46 (0)31–772 5546
Fax: +46 (0)31–772 5590
Email: daria.dallolio@chalmers.se

Printed by Chalmers Reproservice
Chalmers University of Technology
Gothenburg, Sweden 2020

To Leonida and Piero

Magnetic fields around massive protostars as traced by masers and dust emission

DARIA DALL'OLIO
Department of Space, Earth and Environment
Chalmers University of Technology

Abstract

It is not fully clear how the magnetic field acts during the first stages of star formation. A possible way to clarify its role is to observe the polarized light coming from masers and thermal dust emission. By measuring linear polarization angles and Zeeman splitting of different maser species it is possible to study the magnetic field morphology and strength in different parts of the protostar. Polarized emission of thermal dust has also been used extensively to probe the magnetic field at the onset of star formation.

In this thesis we study the magnetic field properties of two well-known sources: the massive protostar IRAS 18089-1732, showing a hot core chemistry and a disc-outflow system, and the high-mass star forming complex G9.62+0.19, presenting several cores at different evolutionary stages. We also investigate the polarization properties of selected methanol masers, considering newly-calculated methanol g-factors and hyperfine components. We compare our results with previous maser observations and we evaluate the contribution of preferred hyperfine pumping and non-Zeeman effects.

We make use of MERLIN and ALMA observations and we analyse the polarized emission by 6.7 GHz methanol masers and thermal dust. Simulations were run using the radiative transfer code CHAMP for different magnetic field values, hyperfine components and pumping efficiencies.

We observe that the large scale field probed by dust continuum emission is consistent with the small scale magnetic field probed by masers. Moreover, in the G9.62+0.19 complex we resolved several cores showing polarized emission. We propose an evolutionary sequence of magnetic field in this complex, where the less evolved stellar embryo exhibits a magnetic field stronger than the more evolved one. From our simulations, we find that preferred hyperfine pumping can explain some high levels of linear and circular polarization. We also notice that non-Zeeman effects need to be considered in magnetic field studies.

In conclusion, our work indicates that there is a link between the magnetic field at different scales. More masers observations will help in evaluating the relevance of non-Zeeman effects and obtain good estimates of magnetic fields close to the protostar. Future multi-wavelength and multi-scale observations, aimed at detecting polarized light from masers, thermal dust and thermal molecular lines, will help to constrain magnetic field properties around massive protostars.

Keywords: magnetic field – stars: formation – stars: massive – masers – dust – polarization – stars: individual: IRAS 18089-1732 – G9.62+0.19

Research contributions

This thesis is based on the work contained in the following papers:

- D. Dall'Olio, W. H. T. Vlemmings, G. Surcis, H. Beuther, B. Lankhaar, M. V. Persson, A. M. S. Richards, and E. Varenius:
  Methanol masers reveal the magnetic field of the high mass protostar IRAS 18089-1732
  Astronomy & Astrophysics, 607, A111 (2017).

- D. Dall'Olio, W. H. T. Vlemmings, M. V. Persson, F. O. Alves, H. Beuther, J. M. Girart, G. Surcis, J. M. Torrelles, and H. J. Van Langevelde:
  ALMA reveals the magnetic field evolution in the high-mass star forming complex G9.62+0.19
  Astronomy & Astrophysics, 626, A36 (2019).

- D. Dall'Olio, W. H. T. Vlemmings, B. Lankhaar and G. Surcis:
  Polarization properties of methanol masers
  Manuscript submitted to Astronomy & Astrophysics.

Other publications not included in this thesis

- W. H. T. Vlemmings, B. Lankhaar, P. Cazzoletti, C. Ceccobello, D. Dall'Olio, E. F. van Dishoeck, S. Facchini, E. M. L. Humphreys, M. V. Persson, L. Testi, J. P. Williams
  Stringent limits on the magnetic field strength in the disc of TW Hya. ALMA observations of CN polarisation.
  Astronomy & Astrophysics, 624, L7 (2019).

Papers on science education

- D. Dall'Olio and P. Ranalli:
  Costellazione Manga: explaining astronomy using Japanese comics and animation.
  Communicating Astronomy with the Public Journal IAU–OAO, 24, 7 (2018);

- EVN Radionet3 QueSera group:
  Eagle View Network
  Editoriale Scienza, Oct. 2015;

- D. Dall'Olio:
  Costellazione Manga: le stelle nel fumetto e nel cinema di animazione giapponese
  Giornale di Astronomia, vol.41, no.1, Fabrizio Serra Editore, Mar. 2015.

Contents

Chapter 1

Introduction

The formation and early evolution of stars is the subject of active studies in astrophysical research. It encompasses complex physical and chemical processes which are not yet completely understood, and it offers a number of still open questions. A star is mostly made up of hydrogen and helium; heavier elements are present for a few per cent of the total mass and they are the outcome of nuclear fusion that occurred in stars of previous generations (Fig. 1.1). The star formation phase is the stage when the stellar mass is determined. The stellar mass and metallicity are important parameters, because they determine the path of stellar evolution.
In particular, massive stars can explode as Type II Supernovae (SN), enriching the surrounding medium of newly-produced material and driving the structure and the chemical evolution of the host galaxy. Moreover massive stars heavily influence their surrounding producing ionizing ultra-violet (UV) radiation, along with stellar winds, and eventually Supernovae shocks and therefore they actively concur to reshape and heat the interstellar medium (ISM). These phenomena can indeed trigger the formation of new stars, or destroy the clouds of gas suppressing the star formation process. Also low-mass stars undergo various stages of mass loss, for example during the giant phase or the planetary nebula stage. Moreover, stellar nurseries are also the places where complex organic molecules and planets are created. Therefore, answering the questions about stellar birth can shed some light on our own origins.
A wide range of problems needs to be investigated, and just a few examples of outstanding questions waiting for solutions are:
what are the conditions under which a cloud fragments, to form stellar associations or clusters? Are high- and low-mass stars formed by the same processes? What mechanisms govern the production and evolution of discs, jets, and outflows? What role has magneto-hydrodynamics (MHD) in all these phenomena?
This thesis will focus on investigating the role played by magnetic fields at the onset of high-mass star formation. The dramatic changes that occur in the deeply

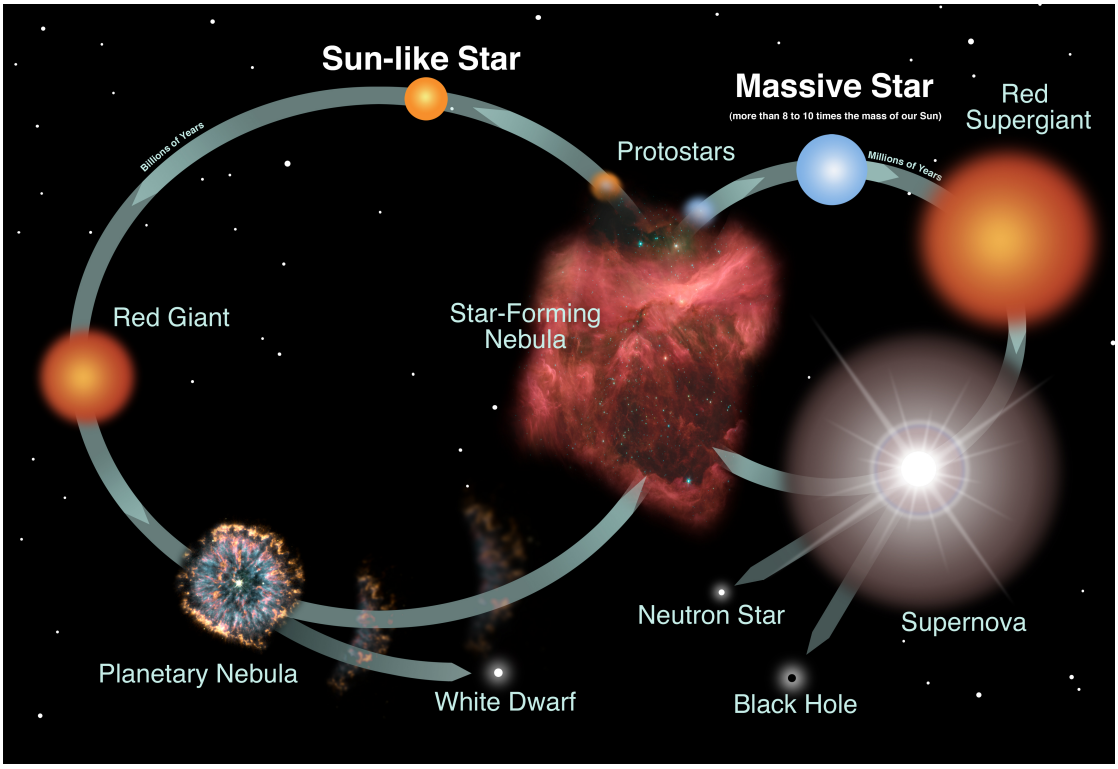

Figure 1.1: Illustration showing the life-cycle of Sun-like and massive stars. Star forming regions are the place where new stars are generated. At the end of their evolution the stars return enriched material to the interstellar medium; a new generation of stars can form from the debris of the previous ones. (Credits: NASA and the Night Sky Network).

magnetized ISM and that lead to the dissipation of the magnetic field in a newborn star are still uncertain. As a consequence, the link between the magnetic field and the physical dynamics of a pre-stellar embryo is also unclear. In order to study these processes, we need to peek inside the stellar nurseries, the molecular clouds, looking for the smaller structures such as pre-stellar cores, outflows and discs.

For this purpose, observations of maser and dust polarized emissions are extremely valuable since they can reveal the morphology and the strength of the magnetic field, probing and mapping the field close to the protostar.

Masers (microwave amplification by the stimulated emission of radiation) are the microwave counterpart of lasers, based on the quantum theory concept of stimulated emission, and they are commonly observed in the Universe. Maser polarization observations are extremely important since they can probe and map the field close to the protostar. Many molecules such as water, methanol, OH, and SiO present maser emissions. Masers show a typical set of strong and narrow lines in the spectrum, and thanks to their collimated emissions, they are powerful tools to

reveal the magnetic field morphology at the small scales of few astronomical units (au) around protostars. Polarized emission from dust has been extensively used to probe the magnetic field at the early stages of star formation. The polarization can indeed be produced by the alignment of dust grains with their long axes perpendicular to the magnetic field.

The birth of a star always happens in the darkness of cosmic dust: stars forms in optically thick clouds, where dust absorbs most of the visible light. Therefore, when a newborn star finally becomes visible at optical frequencies, stellar winds have removed most of the dust and the formation processes that we are interested in has already stopped. Thus to study the embedded stellar nurseries we need to use a telescope sensitive at the wavelengths where the surrounding material is transparent. This is possible by observing in the wavelength range from cm to sub-mm (in the radio and microwave regions of the electromagnetic spectrum) and the required high resolution is obtained with interferometers (e.g. MERLIN and ALMA).

The structure of this thesis is as follows. I will briefly introduce magnetic fields in star forming regions in Chap. 2. I will describe masers and dust polarization observations and their importance to understand magnetic fields in star formation process in Chap. 3 and Chap. 4. I will briefly discuss instruments and observations in Chap. 5. A short introduction to the appended papers and follow-up ideas may be found in Chap. 6 and the future prospects are presented in Chap. 7.

Chapter 2

Magnetic fields in massive star formation

Over the past decades, the role played by magnetic fields during massive star formation has been a topic of great debate.
While some works showed that magnetic fields can significantly influence each stage of massive star formation (Mouschovias et al. 2006; Tan et al. 2013; Tassis et al. 2014; Klassen et al. 2017), other authors considered the effect of turbulence and gravity more important (Vázquez-Semadeni et al. 2011; Wang et al. 2014).
The magnetic field morphology around massive protostars has been probed, e.g. using masers and dust, only in a limited number of sources (Crutcher & Kemball 2019; Hull & Zhang 2019). This is partially due to the observational challenges in identifying high mass protostars, since they are rare and they evolve quickly ($\sim 10^5$ yr). Protostellar cores are also embedded in dark clouds, typically located at fairly large distances from us. They often form in dense clusters where the cores are only separated by few arcsecs, making it more difficult to study the effects and influences of single and isolated stars separately. Moreover high-mass stars start to burn hydrogen before the conclusion of the accretion stage, resulting in a further challenge when trying to disentangle the intrinsic luminosity of the protostar from the luminosity due to the accretion.
Therefore, many questions are still waiting for an answer. How do magnetic fields influence the fragmentation of the molecular cloud? What is the importance of magnetic fields in core collapse? What is the relationship between feedback phenomena and magnetic fields? Are magnetic fields dynamically important with respect to gravity and turbulence?
Some theoretical simulations illustrated that magnetic fields can affect fragmentation, slow down cloud collapse, influence accretion, and drive feedback phenomena such as collimated outflows which are important in removing excess angular momentum (for a comprehensive review see Hennebelle & Inutsuka 2019; Krumholz & Federrath 2019; Teyssier & Commerçon 2019). In some models, magnetic fields are also required to stabilize discs and to allow for the large accretion rates nec-

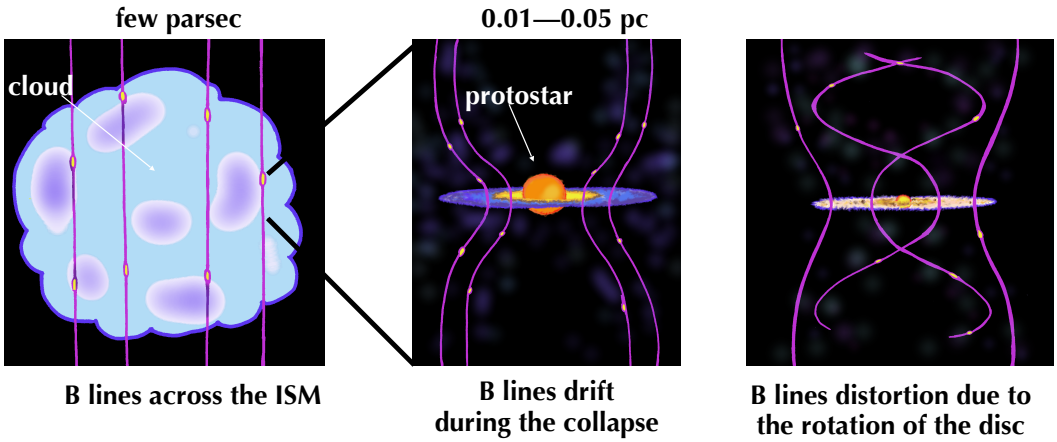

Figure 2.1: A cartoon of the main steps of star formation, where the magnetic field lines (B lines) are drawn in pink. Some models show that B lines could be drifted and distorted during the collapse of the initial cloud and during the accretion of material onto the protostar, but observational proofs of this theory are still poor. (Credit: D. Dall'Olio).

essary during massive star formation (Johansen & Levin 2008; Stepanovs et al. 2014); they are thought to play a key role in both the envelope evolution and the jet launching, which are crucial elements in the earliest stages of star and planet formation (for a recent review see Wurster & Li 2018; Pudritz & Ray 2019).

However, it is still unclear what mechanism can dissipate the strong magnetic field normally observed in the ISM but almost absent in stars. Indeed if all of the magnetic flux that threads a typical star-forming dense core was dragged into the central object, then the stellar field strength would be orders of magnitude stronger than the observed value (Shu et al. 1987). A possible explanation can be given by non-ideal MHD effects such as *ambipolar diffusion* (Mouschovias 1976; Krasnopolsky & Gammie 2005; Vázquez-Semadeni et al. 2005) and *Ohmic dissipation* (Shu et al. 2006; Gonçalves et al. 2008).

In magnetically regulated star formation simulations, the collapse occurs when gravitational forces prevail over the magnetic and gas pressures. Then, since the collapsing gas experiences extreme compression (from $\sim 10^{18}$ to $\sim 10^{11}$ cm), the density increases drastically (a factor of $\sim 10^{21}$), and the angular momentum must be transferred from the collapsing material to the surrounding cloud. Eventually, the forming protostar must dissipate the magnetic field initially present in the collapsing gas.

The ISM inside a molecular cloud is known to be strongly magnetized. The plasma (composed by electrons, protons, charged dust grains and ions) is deeply coupled to the magnetic field: the magnetic field lines are said to be *frozen* into the fluid and build a net that supports the gas against the collapse (see Fig. 2.1, left panel). Also,

the charged particles circle around the magnetic field lines, colliding with other neutral particles in the surrounding molecular cloud and acting against the collapse. In addition, magnetic turbulence, which propagates magneto-hydrodynamic Alfvén waves, contributes to counteract gravity. Their effects however cannot last for long. Phenomena such as ambipolar diffusion and Ohmic dissipation operate to dissipate the magnetic flux by several (~ 5) orders of magnitude.

When the fractional ionization is low, as for examples inside a dense MC, the neutral matter is only loosely coupled to the ionized matter. The ambipolar diffusion makes the neutrals decouple from the charged particles; the neutrals, not being bound by the frozen magnetic field, start to slowly move past the magnetic field lines and collapse under the influence of the gravity (Mestel & Spitzer 1956). Ohmic dissipation acts similarly, but converting the magnetic energy in thermal energy: some residual coupling still remains and because of this, when the neutrals collapse, the magnetic field lines in opposite directions are pressed together. When the field lines reconnect, energy is released in form of heat.

However, it is not yet clear which process dominates between Ohmic dissipation and ambipolar diffusion; it probably depends on the magnitude of the initial magnetic energy density relative to the gravitational and turbulent energy density and the initial magnetic field configuration.

As the collapse proceeds (Fig. 2.1, central panel), the gas accumulates and deforms the magnetic field lines towards the centre of the core, generating a hourglass shape, with a symmetry axis perpendicular to the major axis of a flattened disc of ~ 1000 au (Galli & Shu 1993a,b; Allen et al. 2003; Gonçalves et al. 2008; Mocz et al. 2017). And indeed, the predicted hourglass has been detected in a few massive protostars (Girart et al. 2009; Qiu et al. 2014; Li et al. 2015). For example, Fig. 2.2 shows the magnetic field maps of W51 e2 and e8 observed by SMA and by ALMA at various spatial resolutions. The e2 core presents a hourglass morphology at a resolution of $\sim$3000 au (top middle panel), and other substructures are visible at resolution of $\sim$1500 au (top right panel), possibly due to the action of the ongoing gravitational collapse that pulls the magnetic field lines (Koch et al. 2018).

The fraction of objects presenting hourglass shapes seems to be small (21% according to Hull & Zhang 2019), but this can be an effect of the projection on the line of sight, as suggested by Girart et al. (2013): indeed, considering the geometry of the protostar, a pinched magnetic field configuration can generate a wide range of magnetic field morphologies. However, as pointed out by Hull & Zhang (2019), the few sources currently observed with ALMA show either very chaotic morphologies, appearing more influenced by turbulence and infall processes, or morphologies shaped by outflows (Maury et al. 2018), making the scenario even more challenging to interpret.

Probing magnetic fields in accretion disc and outflows is also arduous, and there are still open questions regarding their formation and their alignment with the field lines. Therefore, understanding how the magnetic field is linked to the accre-

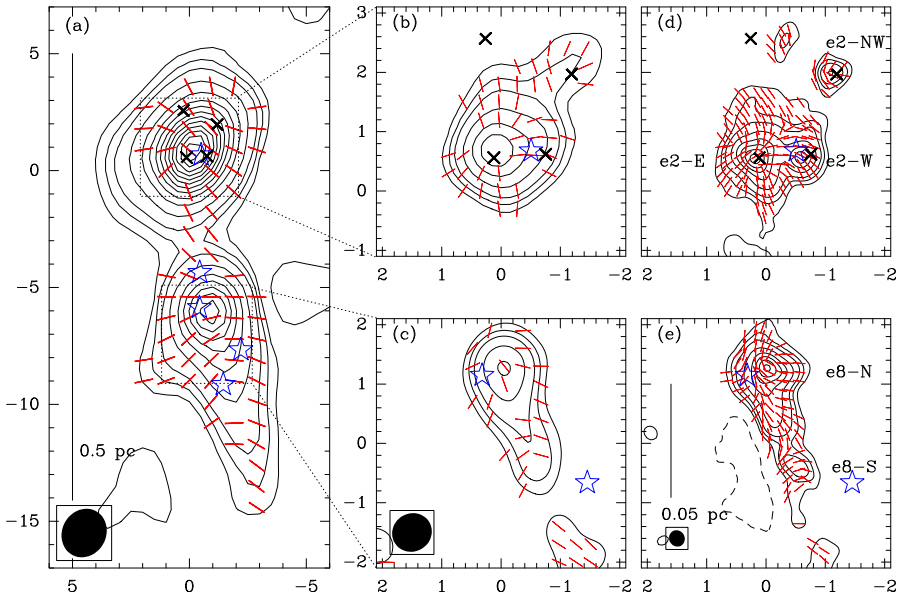

Figure 2.2: Red line segments indicate magnetic fields in the W51 complex, around the source e2 and e8. Left panels: SMA observations (870 μm) at a resolution of ∼10000 au (panel a), and ∼ 3500 au (panels b and c). Right panels: ALMA observations (1.3 mm) at a resolution of ∼1300 au (panel d and e). Black contours indicates total intensity at levels 3, 6, 10, 20, 35, 50, 65, 80, 95 times 75 mJy beam^{-1}, 60 mJy beam^{-1}, 6 mJy beam^{-1} respectively. × symbols mark the known continuum sources W51 e2-E, e2-W, e2-NW, and e2-N. Star symbols indicate known ultra-compact HII regions. The black ellipses in the lower left corner are the synthesized beams. Figure from Koch et al. (2018).

tion mechanisms, angular momentum transport and outflows and jets launching is another key issue.

If the angular momentum is conserved, then the contraction cannot occur. Thus the angular momentum must be transferred from the collapsing gas to the nearby material, which disposes itself in a protostellar disc. Assuming that the rotation axis is parallel to the direction of the magnetic field, magnetic torques arise generating *magnetic braking*, which transfers the angular momentum to the matter along the equatorial plane creating a rotating disc (Allen et al. 2003).

Under the effect of a non-uniform rotation caused by the ongoing collapse, an inevitable twisting of the magnetic fields lines appears when the gas starts to condense along them. Fig. 2.1, right panel, illustrates how the cloud core rotation can distort the magnetic field lines.

Meanwhile, the gas from the surrounding envelope falls onto the accretion disc and is then funnelled onto the protostar. But not all the accreting material from the disc reaches the protostar. A significant portion is launched along the magnetic

fields lines, from the poles of the star in high-speed collimated jets, and another portion is ejected via wide open outflows starting from the plane of the disc. Jet phenomena can be originated by magnetically-driven and collimated disc winds (the models involve magnetic field lines and different regions of the disc, and centrifugal forces that can launch material).
Masers observations are specifically valuable to constrain magnetic fields in these critical regions such as discs and outflows (see Chap. 3). EVN observations of 6.7 GHz methanol masers conducted on a large sample of high mass protostars showed a correlation between the magnetic field and the outflow direction (Surcis et al. 2012, 2013, 2015, 2019). Also in the case of Cepheus A, magnetic fields appear to be aligned with the outflow (Vlemmings et al. 2010), while in DR21(OH) the methanol maser distribution seems to trace a Keplerian disc (Harvey-Smith et al. 2008). In addition, some works show a consistency between the magnetic field inferred by masers and that traced by dust (e.g. W51-e2 and IRAS18089 Surcis et al. 2012; Dall'Olio et al. 2017). In particular, methanol masers probe not just single isolated regions of dense shocked material, but a coherent magnetic field (e.g. Cepheus A and W75N Surcis et al. 2009; Vlemmings et al. 2010).
Maser observations seem to indicate that magnetic fields are dynamically important compared to gravity and angular momentum, from the core to the disc scales. However, dust observations reveal a random alignment between magnetic field and outflows, suggesting that the angular momentum in disc is not determined by the magnetic field orientation (Zhang et al. 2014). Though, dust observations of these regions, as suggested by Girart et al. (2018), may be contaminated by self-scattering of large dust grains (Kataoka et al. 2017) and therefore polarized emission should be analysed carefully.
In any case, the sample of observed massive protostars remains small, and magnetic field parameters are still poorly constrained, in particular at small scales and in the initial stages of massive star formation.
Therefore, in order to build a complete picture of the situation and to understand the magnetic field role in all these processes, more observational constraints are needed. In particular, it is fundamental to observe star forming regions at different evolutionary stages and across different spatial scales. The study of different protostars at different evolutionary stages will give an overview of the magnetic field evolution in time and of the changes that will occur during the star formation path. Moreover, investigating several spatial scales, spanning from cloud scales (100 pc), clump (1 pc), dense core (0.1 pc), protostellar envelope (1,000 au) disc (100 au) and individual star (10 au), will characterize the importance and the influence of the magnetic field in different star forming environments. Checking the consistency of the magnetic field orientation across multiple spatial scales would be an excellent test to reveal the action of strong magnetic fields, compared to other dynamical effects.

Chapter 3

Astrophysical Masers

3.1 Basic theory

The Microwave Amplification by Stimulated Emission of Radiation (MASER) is based on the concept of *stimulated emission* from quantum theory, introduced by A. Einstein in 1917. The first maser device was developed in laboratory only in 1954 by J. Gordon, H. Zeiger and C. Townes, while the first astronomical observation was obtained by Weaver et al. (1965).
A simple representation of the phenomenon is shown in Fig. 3.1: a photon of wavelength λ is incident on an atom or a molecule presenting already the electrons in an excited energy state (panel a). The photon is not absorbed by the molecule but instead it stimulates an excited electron to decay in a lower energy state, by emitting another photon of identical wavelength λ and phase (panel b). The stimulated emission can amplify the signal coming from an originally weak source. The two photons indeed can stimulate emission from two other molecules (panel c) and the process continues causing a chain of reactions that doubles the number of photons each time (panel d). When all the molecules simultaneously decay to the lower energy levels, the maser occurs generating a narrow and bright beam of coherent and monochromatic light (panel e). The radiation intensity rises exponentially and propagates where the molecules present the same velocity, until the upper level begins to depopulate, and eventually the amplification saturates.
In order to understand how the stimulated emission works, we can consider the simplest case of a molecule with only two discrete energy levels, upper (u) and lower (l).
The Boltzmann equation

$$\frac{N_u}{N_l} = \frac{w_u}{w_l} \frac{e^{-\left(\frac{E_u}{kT}\right)}}{e^{-\left(\frac{E_l}{kT}\right)}} \tag{3.1}$$

is valid under thermodynamic equilibrium, and gives the ratio between the electron

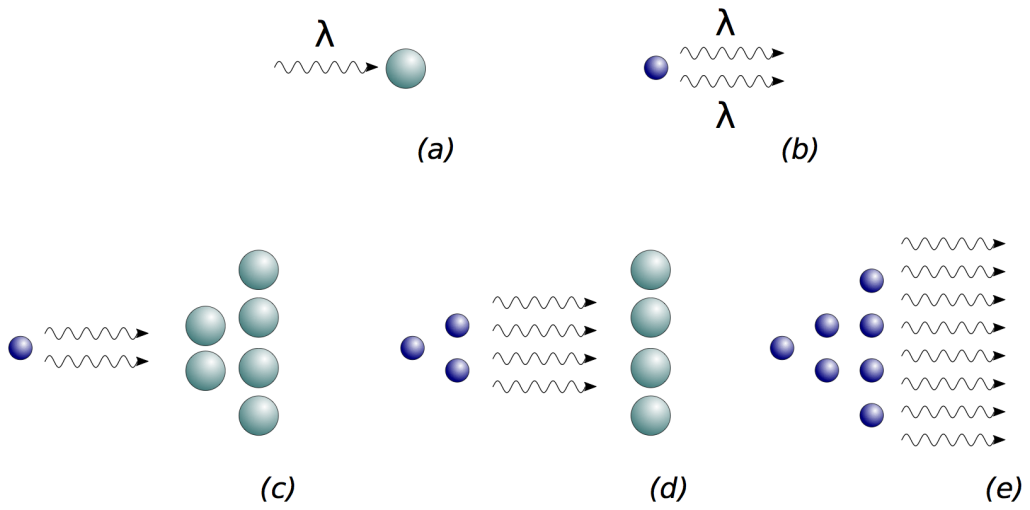

Figure 3.1: Stimulated emission is the physical process motivating masers. In this figure a schematic view of the amplification of the radiation starting from a incident photon on an excited molecules (a) which stimulates the emission of an identical photon (b) and generates a chain of reactions (c-e) causing the maser (see Chap. 3). (Credit: D. Dall'Olio).

population (N) in the two energy states E, where the w's are the statistical weights of the two levels, T is the temperature, and k is the Boltzmann constant.

In environments such as the cold and dense interstellar clouds, the Boltzmann formula predicts $N_l \gg N_u$. Therefore to make the stimulated emission occur, an efficient external source of energy must be present, exciting (*pumping*) the gaseous environment and causing the overpopulation of the upper level of a molecular transition (*population inversion*). Thus the pumping brings the gas in a non-equilibrium state, necessary for the maser amplification, where

$$\frac{N_u}{w_u} > \frac{N_l}{w_l} \quad . \tag{3.2}$$

Masers are associated to various environments such as star forming regions, unstable atmosphere of evolved stars, planetary nebulae, supernova remnants, AGN, planetary atmospheres and comets. Embedded young stellar objects offer several pumping mechanisms from which the maser may arise: stellar wind and the associated shocks, far-infrared radiation from heated dust, and also jets and outflows may provide the energy and the right conditions to stimulate emissions from many different molecular species (e.g. H_2O, OH, CH_3OH and SiO).

3.2 Maser sources in massive star formation

Generally, high-mass star forming regions are efficient producers of maser emissions, since they present enough gain length to amplify radiation to a brightness that makes it observable. Masers are also detected in low mass protostars often associate with jets and shocks (e.g. Moscadelli et al. 2006; Rodríguez-Garza et al. 2017; Kalenskii et al. 2018), but they are less common.

Hydroxyl, water and methanol maser species are largely associated with high-mass star forming region (Elitzur 1992; Gray 2012), and each of them probes different physical conditions, that can arise at different evolutionary stages of the protostars. Therefore, combined studies of different maser species and chemical evolution can help delineate an evolutionary sequence of massive stars. Water masers, for example, can be used to trace high-density, shocked regions like the outflow (e.g. Moscadelli et al. 2005; Lekht et al. 2007; Goddi et al. 2011; Chibueze et al. 2012, and references therein), while hydroxyl masers can trace less dense regions, such as the dusty molecular envelope surrounding the central protostar (e.g. Green et al. 2015; Caswell et al. 2011). Class I and class II methanol masers (Menten 1991) are also found in different regions of the protostar and trace various physical conditions typical of a specific life-stage of young stellar objects (de Villiers et al. 2015; Ilee et al. 2016; Matsumoto et al. 2014) and therefore can be used to infer an evolutionary sequence.

According to Gray (2012), masers in star forming regions can be classified in "early" and "late" types, depending on the evolutionary stage of the hosting protostar and the physical mechanisms that contribute to the pumping process.

The early type masers arise as a consequence of strong shocks in high density and hot regions and the population inversion occurs predominantly through molecular collisions. Spontaneous decay only contributes to their pumping with a small amount of radiative energy. Usually they are associated with the molecular outflows that generate strong shocks when impacting the surrounding ISM of the parental cloud. Bipolar outflows are typical of the first stages of star formation, and therefore these masers usually dissipate when the protostar evolves. They might coexist with the late type only on different spatial scales (e.g. jets and disc) in the intermediate evolutionary stages of the prestellar core.

One of the most frequently observed early type maser is the 22 GHz water maser that was extensively used to infer important information on the kinematics and the morphology of the bipolar outflows in massive star formation (e.g. Moscadelli et al. 2017; Kim et al. 2020; Moscadelli et al. 2020; Chibueze et al. 2020, and references therein). An example is shown in Fig. 3.2, reporting water maser observations in VLA2, one of the massive protostars in the W75N complex. The water masers trace a shock-excited shell of $\sim$185 au diameter, radially expanding with respect to a central source. Water masers were detected in different epochs showing the evolution of the outflow across $\sim$25 years. This shell has evolved from an almost

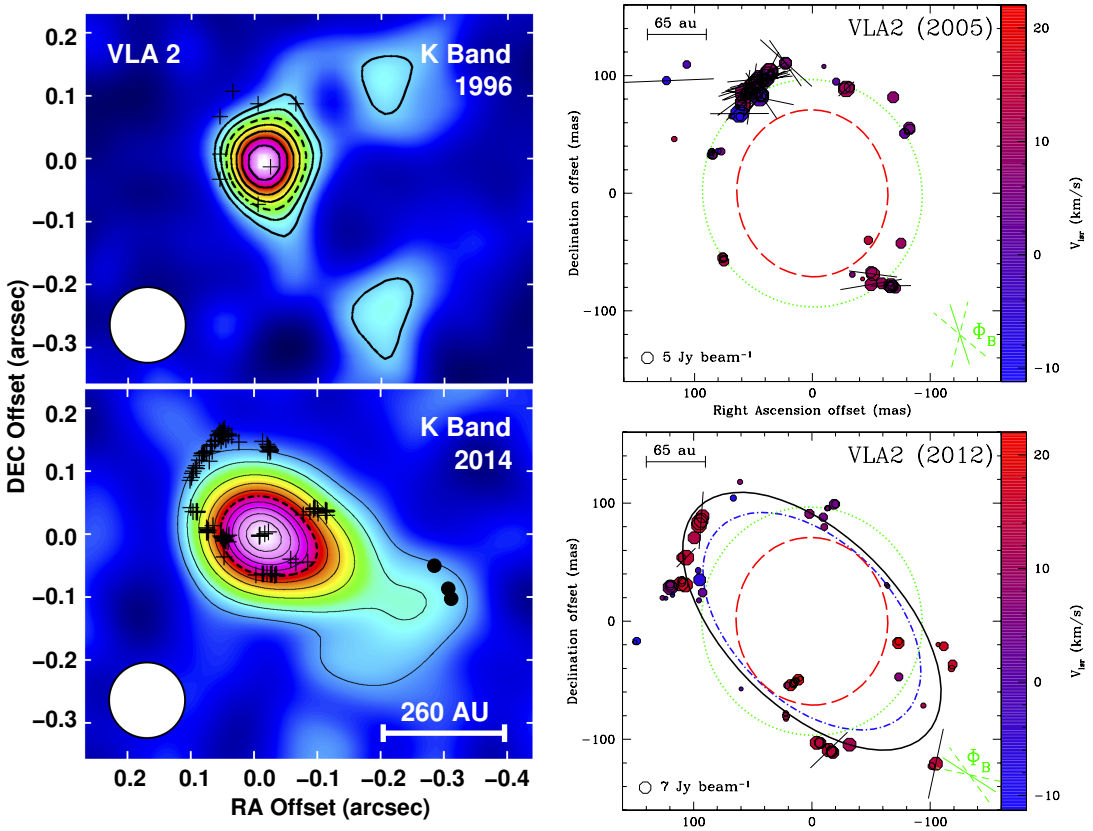

Figure 3.2: Examples of water maser observations in the massive protostar VLA2 in the W75N complex. **Left:** comparison of the K band continuum emission of VLA 2 in epochs 1996 (top left) and 2014 (bottom left) from Carrasco-González et al. (2015). The (0,0) position is RA(J2000)=20h38m36.486s, DEC(J2000)=42°37′34.09″ (±0.03″). Contours are 30, 40, 50, 60, 70, 80, and 90% of the peak intensity in 1996 (1.42 mJy beam^{-1}, rms=150 μJy beam^{-1}), and 5, 10, 20, 30, 40, 50, 60, 70, 80, and 90% of the peak intensity in 2014 (0.82 mJy^{-1}, rms=10 μJy beam^{-1}). Both maps were obtained with the same restoring circular beam of 0.12″ (shown in the bottom left corner of each panel). The water maser positions (plus symbols) are shown for epochs 1996 and 2014 as observed with the VLA by Torrelles et al. (1997) and Carrasco-González et al. (2015), respectively. The positions of the methanol masers for epoch 2014 (black dots) are also indicated. **Right:** comparison of the water maser features around the radio source VLA 2 in 2005 (top right) and 2012 (bottom right) from Surcis et al. (2014). The maser LSR radial velocity is indicated by the colour scale, and the maser flux by the symbol size. Two symbols showing 5 and 7 Jy beam^{-1} are plotted for illustration in the top and bottom right panels, respectively. The linear polarization vectors are overplotted and in the bottom right corner the green vector mark the direction of the magnetic field. The ellipses are the results of the best fit of the water masers detected by Torrelles et al. (2003) (red dashed ellipse epoch 1999), by Surcis et al. (2011a) (green dotted ellipse, epoch 2005), Kim et al. (2013) (blue dot-dashed ellipse) and Surcis et al. (2014) (black solid ellipse).The reference position is RA(J2000)=20h 38m 36.435s, DEC(J2000)=42° 37′ 34.84″.

circular structure to an elliptical one (∼354×190 au) which is oriented with the ordered large-scale (2000 au) magnetic field observed in the region and confirmed by maser polarization observations (Carrasco-González et al. 2015; Surcis et al. 2014; Torrelles et al. 2003). Therefore masers can be reliably used to test the morphology of a young star and its potential disc-outflow system.

Class I methanol masers are also collisionally excited and are associated with shocked H_2 knots in the molecular outflow (e.g. Leurini et al. 2016). While water masers form at the peak of the outflow, class I methanol masers arise on the edges of the outflow (Voronkov et al. 2006). Class I methanol masers include transitions at 25, 36 and 44 GHz (Barrett et al. 1971; Morimoto et al. 1985). They are routinely used as sign of star formation. In particular they are good tools to probe the first evolutionary stages of massive protostars, when it is complicated to observe the outflow activity due to the high extinction in the mid-infrared regime (Leurini & Menten 2017; Breen et al. 2019a). It has been suggested that class I methanol masers form in a later evolutionary stage than the water maser (Reid 2007). However, this is still an open issue, because water and methanol are both associated to shocked gas and their suggested origin is evaporation from grain mantles. In the pre-shocked gas, they are likely bound to the grain mantles but on separate layers, since they accumulate on the dust surface when the molecular cloud reaches different temperatures. It is believed that water accumulates at higher temperature than methanol, and thus it sediments deeper than methanol. Therefore, it means that on average water is released later than methanol (Gray 2012) and under this scenario class I methanol masers would happen before water masers. Other early type masers include H_2CO, CH and NH_3, which we do not discuss in this thesis.

The late type masers are radiatively excited by IR emission from warm dust. Usually, warm dust that occupies the surroundings of the HII region and the accretion disc absorbs the UV radiation produced by the protostar, and thermally re-emits it as IR radiation. Late type masers include OH and class II methanol masers.

Class II methanol masers, such as its brightest 6.7 GHz transition, are widely used as star formation tracers. In particular, several surveys (e.g. the Methanol MultiBeam Survey Caswell et al. 2010; Breen et al. 2015; Paulson & Pandian 2020 or ATLASGAL/ALMA Chibueze et al. 2017) confirmed that the 6.7 GHz maser can be considered a unique tool to probe high-mass protostars. Class II methanol masers includes also other transitions such as the 12.2, 23.1, 37.7 GHz ones. They are mainly spotted in well-ordered linear arrangements along circumstellar discs, and they are believed to be earlier on the evolutionary sequence than OH maser (Minier et al. 2005). 6.7 GHz methanol masers can arise in evolved hot cores that have already developed an outflow (de Villiers et al. 2015) and therefore can be associated to class I methanol masers (Bayandina et al. 2012).

OH masers have been mostly associated to ultra compact HII regions, typically

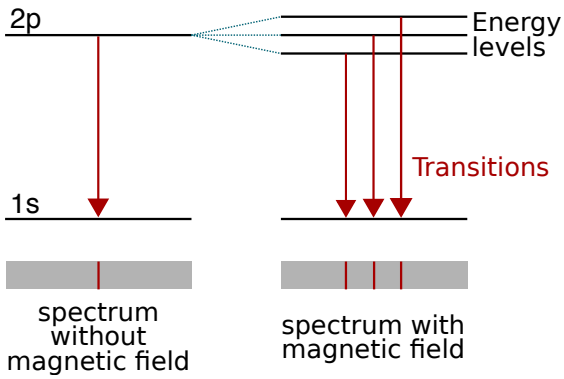

Figure 3.3: Zeeman effect: under the action of a magnetic field, the spectral lines of a molecule are separated in several components due to the magnetic sub-levels. (Credit: D. Dall'Olio).

arising in regions between the ionization front and the expansion shock (Caswell 2004; Ruiz-Velasco et al. 2016). Some works have shown that they can form also at earlier stages, associated to outflows and circumstellar discs (Edris et al. 2017). However, OH masers seem to appear spatially separated and at a later phase than the class II methanol masers. This is probably due to the fact that water is the most probable source of OH, and that it is released from the dust grains after methanol.

3.3 Polarization

Through the study of linearly and circularly polarized maser emission, it is possible to obtain information about the small-scale magnetic field B, such as its direction and strength.

Masers present narrow and bright spectral lines ideal to detect the Zeeman effect: under the action of a magnetic field, the spectral lines of a molecule are separated in several components due to the magnetic sub-levels. The shift is proportional to the magnetic field strength and it is named Zeeman splitting (Fig. 3.3).

According to the theory (Watson 2008; Dinh-v-Trung 2009) the polarization properties of maser emission are deeply influenced by the radiative conditions of the region where the maser is generated (saturated and unsaturated) and by the nature of the masing molecule (paramagnetic or non-paramagnetic). In addition, maser polarization depends on the ratio between the Zeeman frequency $g\Omega$, the rate of stimulated emission R and the decay rate of the molecular state Γ (Western & Watson 1984).

The decay rate of the molecular state Γ is difficult to infer and it is typically assumed to be 1 s^{-1} (Vlemmings et al. 2010). The rate of stimulated emission is

given by

$$R \simeq \frac{AkT_B\Delta\Omega}{4\pi h\nu} \quad , \tag{3.3}$$

where A is the Einstein coefficient which depends on the hyperfine transition, k and h are the Boltzmann and Planck constants respectively, ν is the maser frequency. T_B and $\Delta\Omega$ are the maser brightness temperature and beaming solid angle (Vlemmings et al. 2011b).
The Zeeman frequency is defined as

$$g\Omega = \frac{2g\mu B}{\hbar} \quad , \tag{3.4}$$

where B is the magnetic field in G, $\hbar$ is the reduced Planck constant and g is the Landé g-factor (see e.g. Nedoluha & Watson 1990b). In case of paramagnetic molecule (e.g. OH) μ is the Bohr magneton ($\mu_B = e\hbar/2m_ec$) while in case of non-paramagnetic molecule (e.g. H_2O, CH_3OH and SiO) it is the nuclear magneton ($\mu_N = e\hbar/2m_nc$), where e is the electron charge, m_e and m_n are the electron and nucleon mass respectively.
Thus, the magnitude of the Zeeman effect induced by a magnetic field depends on $g\Omega$ and differs between paramagnetic and non-paramagnetic molecules. Since the ratio $\mu_B/\mu_N \sim 10^3$, paramagnetic molecule can show a split three orders of magnitude larger than the non-paramagnetic one (Vlemmings 2007; Gray 2012). Moreover, for paramagnetic molecules, $g\Omega$ is expected to be larger than the intrinsic line width (therefore the Zeeman components are separated and resolved), while for non-paramagnetic molecules $g\Omega$ can be less that the line width (therefore the Zeeman components overlap).
For paramagnetic molecules, magnetic field properties can be directly inferred by the observed linearly and circularly polarized components; thus the observed Zeeman splitting gives with no theoretical ambiguity the magnetic field component along the line of sight, $B_\parallel = B\cos\theta$, with θ defined as the angle between the magnetic field and the line of sight. For non-paramagnetic molecules, the relation between the linear polarization angle and the magnetic field direction is more complicated, and depends not only on the polarization fraction but also on the saturation level. When the rate of stimulated emission R exceeds the decay rate of the molecular state involved Γ, the maser is considered *saturated*.
The presence of a strong and ordered magnetic field is normally responsible of the observed polarization, but there are also other effects that can influence our measurements. In general, other contributions that can compromise the magnetic field measurements can be due to velocity gradients along the maser line, and blending of maser features, giving in both cases an underestimate of the magnetic field strength by about a factor of two. Moreover, when polarized emission passes through a magnetic field, the polarization plane can rotate (Faraday rotation) affecting the polarization angle and therefore the magnetic field measurements.

There is also an internal Faraday rotation, due to the intrinsic characteristic of the maser itself that can alter the polarization feature.
Moreover, there are also other non-Zeeman mechanisms that can generate high levels of polarization, such as instrumental effects, magnetic field changes along the maser path and a rotation of the symmetry axis (Vlemmings et al. 2011b). The latter, in particular, can lead to an overestimation of the magnetic field. When $g\Omega > R$, the magnetic field direction is the quantization axis, but when the maser brightness increases and the maser saturates, R becomes much larger than $g\Omega$ and a rotation of the symmetry axis can happen. This change of quantization axis can produce an intensity-dependent circular polarization almost identical to the regular Zeeman splitting (Nedoluha & Watson 1990a). Therefore it is vital to know when this effect might occur, by estimating R and $g\Omega$.
From Eq. (3.3) and Eq. (3.4), the ratio between the Zeeman splitting rate and the stimulated emission rate is:

$$\frac{R}{g\Omega} = 1.7 \times 10^7 \frac{1}{g} \frac{[\mathrm{mG}]}{B} \frac{T_b}{[10^{10}\mathrm{K}]} \frac{\Delta\Omega}{[10^{-2}\mathrm{sr}]} \frac{[\mathrm{GHz}]}{\nu} \frac{A}{[\mathrm{s}^{-1}]}. \tag{3.5}$$

The rotation of the symmetry axis can happen when $\frac{R}{g\Omega} > 1$.
Therefore, for non-paramagnetic molecules, magnetic field parameters can be obtained only if the two requisites $g\Omega > R$ and $g\Omega > \Gamma$ are satisfied. Under these conditions, the circular polarization is proportional to the magnetic field strength. Otherwise, the magnetic field can be overestimated by up to a factor of four (Nedoluha & Watson 1990a; Pérez-Sánchez & Vlemmings 2013). The linear polarization vectors are parallel to the magnetic field when $\theta < \theta_{crit}$, but they are perpendicular when $\theta > \theta_{crit}$, where $\theta_{crit} \simeq 55^\circ$ is the Van Vleck angle.
Anisotropic pumping can also enhance linear polarized emission in diatomic molecules and in this case the fractional linear polarization p_L will increase with higher angular momentum, due to anisotropic population of the involved magnetic substates (Nedoluha & Watson 1990a; Lankhaar & Vlemmings 2019). Anisotropic pumping can be produced by differences in the angular distribution of the radiation field associated with the population inversion process. Observations of SiO masers presenting $p_L = 100\%$ in the J=1–0 transition and $p_L > 33\%$ for higher J were obtained by Amiri et al. (2012) and Vlemmings et al. (2011a), respectively, confirming that this effect can happen.
In the case of methanol, recent simulations have shown that linear and circular polarization levels can also be enhanced under preferred hyperfine pumping (Dall'Olio et al., submitted), since each hyperfine level reacts differently to the surrounding magnetic field.

3.3.1 Magnetic field observations

Weinreb et al. (1965) reported the first indication of an interstellar Zeeman effect by observing polarization in hydroxyl (OH) masers. Since then, Zeeman splitting

has been detected in several other atoms and molecules such as HI, OH and CN in extended gas; and hydroxyl, methanol (CH_3OH) and water in masers. The Zeeman effect in water masers was first reported by Fiebig & Guesten (1989) and confirmed by Sarma et al. (2001), while the first linear polarization observations for methanol masers was performed by Koo et al. (1988) at 12.2 GHz and by Ellingsen (2002) at 6.7 GHz. The first circular polarization observations of 6.7 GHz methanol masers were made by Vlemmings (2008). Thereafter, several works established that maser emission (from e.g. methanol and water) is a reliable probe to test magnetic fields close to the protostar, at the scale of 100-1000 au (e.g. by Green et al. 2007, Vlemmings et al. 2010, Sarma et al. 2008, Dodson & Moriarty 2012; and Surcis et al. 2019 and their previous papers). It has been demonstrated that maser detections sample a coherent magnetic field and not just isolated regions of dense shocked material.

Polarized radiation can be defined by the four Stokes parameters I, Q, U, V. The quantity I is the specific intensity, Q and U are linked to the linear polarization, while V is connected to the circular polarization. The morphology of the magnetic field can be obtained from the linear polarization. After the data reduction, the U and Q datacubes are combined to produce cubes of linearly polarized intensity (I_P=$\sqrt{Q^2 + U^2 - \sigma_P^2}$) and linear polarization angle ($\psi = 1/2 \times \mathrm{atan}(U/Q)$), where $\sigma_P = \sqrt{[(Q \times \sigma_Q)^2 + (U \times \sigma_U)^2]/(Q^2 + U^2)}$. Then for each maser feature it is possible to measure the median linear polarization fraction and the median linear polarization angle across the spectrum. Taking into account the assumptions made in Sect. 3.3, if the angle between the magnetic field and the line of sight is less than the Van Vleck angle, then the linear polarization is perpendicular to the magnetic field.

The strength of the magnetic field along the line of sight can be inferred by the circular polarization (Vlemmings et al. 2001, 2006; Surcis et al. 2014; Momjian & Sarma 2019; Sarma & Momjian 2020). An example of a V spectrum for a CH_3OH maser feature is given in Fig. 3.4. The observed V spectrum is a sin-shaped function, corresponding to the derivative I′ of the total power spectrum I (Troland & Heiles 1982). By fitting Gaussian components to the I spectrum, and the corresponding derivative to the V spectrum, we can take

$$V = aI + \frac{b}{2}\frac{\mathrm{d}I}{\mathrm{d}\nu} \tag{3.6}$$

where a and $b = zB\cos\theta$ are fit parameters, together with intensity of the Gaussian components, centre velocity, and line width; θ is the angle between the magnetic field and the line of sight, B is the magnetic field strength and $z = 2(\mu_N/h)g$ is the Zeeman splitting factor.

Recently a list of Landé g-factors and α_Z coefficients (where $z = 2\alpha_Z$) has been estimated for the 6.7 GHz and other methanol transitions considering all their possible hyperfine components (Lankhaar et al. 2018).

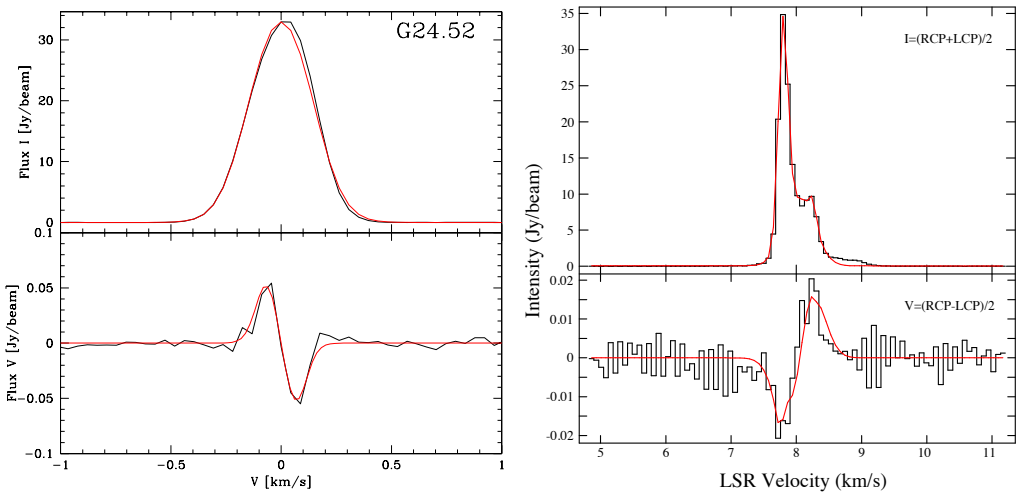

Figure 3.4: Examples of total intensity (I, upper panel) and circularly polarized intensity (V, lower panel) spectra for a CH_3OH maser feature in G24.78+0.08, left panel (Surcis et al. 2015) and in OMC-1, right panel (Sarma & Momjian 2020).

Fig. 3.5, left panel, depicts an artist impression of a massive protostar, where maser observations are providing unique probes of the fine-scale magnetic fields and kinematics of the source. The maser spots are drawn following real observations performed on NGC 7538-IRS1 and W75N (Surcis et al. 2011a,b). Different maser species were detected in various environments of the protostar: from the outer region of the torus to the inner parts closer to the protostar, hydroxyl and methanol masers are tracing various conditions of the disc, while water masers are often associated to the base of the outflow (Surcis et al. 2011b) or tracing the shocked outflow region (Surcis et al. 2011a). Maser observations can probe the presence of magnetic field in regions where the density is $\geq 10^5$ cm^{-3} (Crutcher & Kemball 2019). Fig. 3.5, right panel, shows the magnetic field-density relation obtained by Vlemmings (2008), using Zeeman magnetic field measurements obtained from different masers species.

Zeeman splitting detections in class I methanol maser transitions at 25 GHz, 36 GHz and 44 GHz were seen toward some high mass star forming regions such as M8E, DR21(OH), DR21W, OMC-1 and OMC-2. These observations revealed a magnetic field magnitude of 20–75 mG or stronger, consistent with shock compression scenario (Sarma & Momjian 2009, 2011; Momjian & Sarma 2017, 2019; Sarma & Momjian 2020). Class II methanol masers can probe magnetic fields at densities $\geq 10^6$ cm^{-3} (T$\leq$ 50 K), closer to the protostar (e.g. Wiesemeyer et al. 2004; Bartkiewicz et al. 2009).

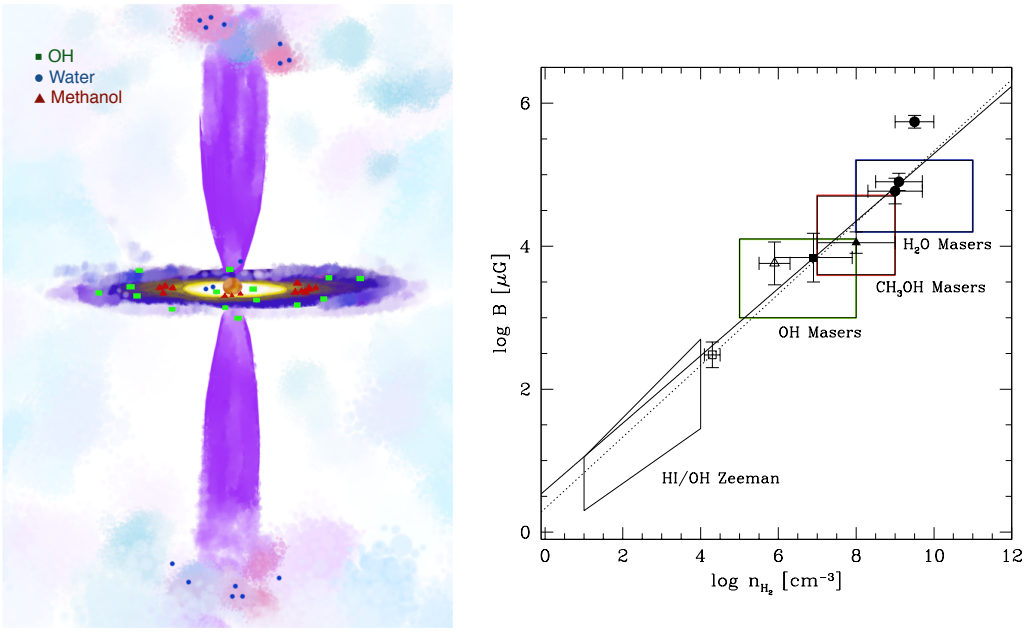

Figure 3.5: Left: artist impression of a massive protostar where different maser species were detected in different environments of the protostar (credit: D. Dall'Olio). Masers observations based on Surcis et al. (2011a,b). Right: magnetic field-density relation in the massive star forming region Cepheus A, from Vlemmings (2008). The points with error bars indicate values inferred by Zeeman splitting measurements from maser observations. The boxes show literature values for masers and extended regions for other protostars. The solid line shows the $B \sim n^{0.5}$ relation, and the dotted line indicates the fit to Cepheus A data.

3.4 Future perspectives

Future observations will offer the possibility to extend the measurements of the magnetic field-density relation over a larger sample of sources. Performing high angular resolution surveys with telescopes like ALMA is fundamental to resolve the population of prestellar cores within massive clumps and explore the association of masers with massive protostars. For example, Chibueze et al. (2017) performed this type of work, comparing the results from the MMB survey for 6.7 GHz methanol masers and ACA observations of massive protostars. They found that $\sim$ 38% of the sample of massive dense cores was associated with methanol masers. Zeeman effect observations are also crucial to draw a complete picture of the role played by magnetic fields in the evolution of molecular clouds and star forming regions.
Currently only a few cases of both masers and dust polarization were observed towards the same regions (e.g. in W51-e2 discussed in Surcis et al. 2012 and IRAS 18089-1732 Dall'Olio et al. 2017). Therefore it is particularly valuable to add more observational evidences that the magnetic field at the small scales probed by masers tracks the field at larger scales, probed e.g. by the dust, and not small-scale fluctuations.

Chapter 4

Dust polarized thermal emission

One of the magnetic field tracers at the typical scales of star-forming cores and envelopes is the polarized thermal emission emitted from dust grains with sizes $< 100\,\mu$m. To produce polarization the grains must be lined up. Recent theories indicate that dust grains are aligned with their major axes perpendicular to magnetic field lines, and therefore from the study of linear polarization it is possible to understand more about the morphology of the magnetic field.

4.1 Dust alignment mechanisms

The theory of grain alignment is a very complex topic and requires a thorough treatment that is beyond the scope of this thesis. Therefore, I give here only a brief introduction, and refer to the extensive reviews by e.g. Lazarian & Hoang (2007) and Andersson et al. (2015).
The population of dust grains is composed by particles of different sizes, ranging from very small ($\sim 0.001 - 0.01\mu$m) to large ($\sim 0.01 - 1\mu$m) bodies. They are usually made of silicates, amorphous carbon and graphite, assembled in simple shapes such as spheroids or cylinders (Compiègne et al. 2011). Inside the colder regions of the molecular clouds they can aggregate in more asymmetric shapes and can store icy mantles of volatile materials. Observations of the polarized emission at different wavelengths showed a wavelength dependence, meaning that the alignment mechanism can vary with grain size and environment (Vaillancourt et al. 2008). Therefore, in order to understand which mechanism is responsible for the dust grain alignment, it is important to know which part of the grain population is involved in the polarization process and also in which environment the process is happening. Currently, the three main grain alignment theories are the radiative alignment (Dolginov & Mitrofanov 1976), the paramagnetic relaxation (Davis & Greenstein 1951) and the mechanical alignment (Gold 1952b,a).
The majority of theoretical works, supported by recent observations of interstellar

dust polarization, suggests that the *radiative alignment torque* (RAT) mechanism produces the best explanation of the dust polarization observed in the optical, infrared and millimetre range (Weingartner & Draine 2003; Lazarian & Hoang 2007). The RAT paradigm shows that under the effect of an anisotropic radiation field, coming for example from an embedded protostar or an external UV source, dust grains are aligned with their major axes perpendicular to magnetic field lines. The anisotropic starlight incident on a dust grain can create a torque that can rotate and align the grains. The rotational axes of the particles precess round the magnetic field direction, while the radiative torque tends to align the grains with their long axes perpendicular to the magnetic field. This alignment is independent from the radiation direction or the magnetic field direction. It seems that RAT works very well for large grains that are usually considered the most relevant for polarization.

Some authors observed an excess of UV polarized emission and considered it an evidence that also grains smaller than ~ 0.05 μm can align. In this case the *paramagnetic relaxation theory* can be used. When the grain is composed by paramagnetic material (like silicates) it can keep is angular momentum fixed and thus minimize the energy by replacing the rotation with up-down flips of its spin. This process is called magnetization and the paramagnetic relaxation theory proposes a relaxation mechanism where the dissipation of the magnetization energy is responsible of the alignment of the spin axis of the silicate grains with the magnetic field (Draine & Fraisse 2009).

In the third theory, *the mechanical alignment* is caused by the interaction of an elongated grain with gas flowing relative to the dust. In this process the grains line up with their angular momenta perpendicular to the flow of gas around dust. This method originally did not include the action of a magnetic field and it is not in fully agreement with observations. Recent revisions of the mechanical alignment included magnetic fields and suggested that this mechanism can be probably active in the strong outflows generated by high mass protostars (Lazarian & Hoang 2007). However this mechanism should be driven by Alfvén waves and has not yet been observed (Andersson et al. 2015).

It is important to mention that two other possible sources of polarized dust emission independent of magnetic fields are dust self-scattering (Kataoka et al. 2015) and radiative torques called k-RATs (Tazaki et al. 2017), that align grains in the direction of the radiation field. The dust self-scattering mechanism affects the polarized emission from sub-millimetre-sized grains that populate the dusty region of e.g. the protoplanetary disc. The degree of polarization relative to dust scattering can be obtained by the intensity observation since it is proportional to the radiation anisotropy. This mechanism acts on small scales of a few tens of au and at densities $> 10^7$ cm^{-3}.

The k-RATS mechanism depends on the grain shape and size. The degree of polarization for grain alignment is given by the grain axis ratio and the alignment

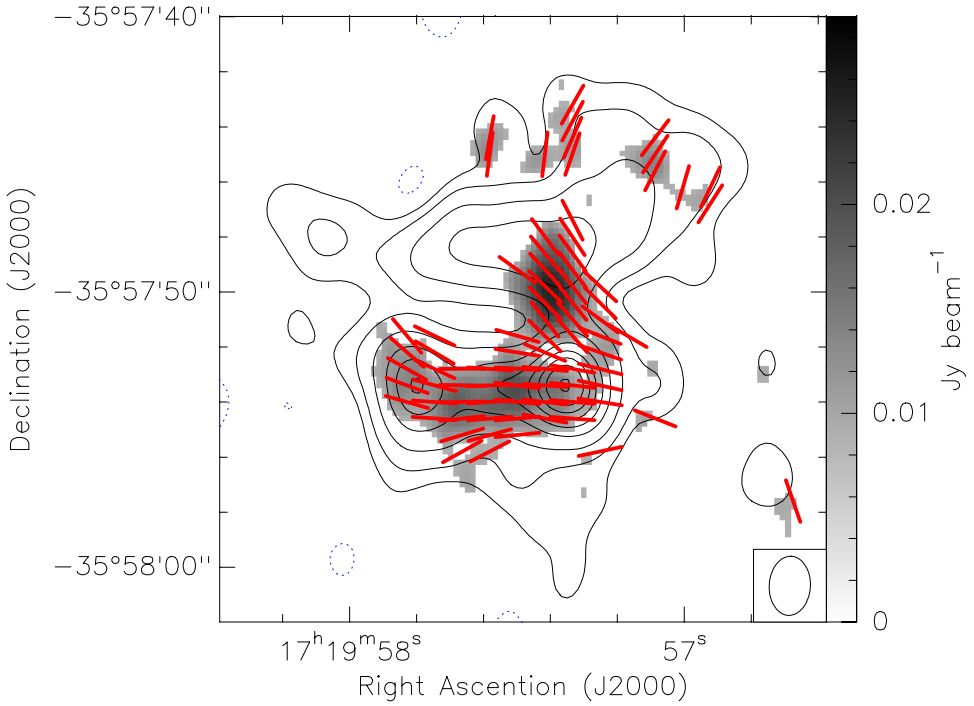

Figure 4.1: NGC 6364 V as seen with SMA (Juárez et al. 2017): image of the 870 μm dust polarization emission overlaid with the contour map of the 870 μm dust continuum emission. The contour levels are -4, 4, 12, 30, 60, ..., 180, 220 times the rms noise (5.5 mJy beam^{-1}). Gray scale shows the polarization intensity in Jy beam^{-1}. The red segments are the inferred magnetic field orientations projected on the plane of the sky.

efficiency (Tazaki et al. 2017). Several observations of protostellar discs performed with ALMA at 3 mm, 1.3 mm and 830 μm showed the polarization patterns consistent with the ones predicted by these two mechanisms (e.g. Kataoka et al. 2017; Stephens et al. 2017). The current k-RATs models suggest that the small grains can result aligned with the magnetic field only in case B>130 mG (Tazaki et al. 2017). However, a consistent polarization pattern at 3 mm, 1.3 mm and 830 μm wavelength can be a signature of the magnetic field acting on grain alignment, as showed by Alves et al. (2018).
When the number densities are lower than those found inside the protoplanetary discs (e.g. $\sim 10^4 - 10^6$ cm^{-3}), the information on the structure of the magnetic field can be extracted by studying the linearly polarized dust emission. In Fig. 4.1 and Fig. 4.2 two examples are given of thermal emission of polarized dust from recent observations of star forming cores in the NGC 6364 V region (Juárez et al. 2017) and in the IRDC 18310-4 clump (Beuther et al. 2018). Dust polarization can be also related to the magnetic field strength by using the Davis-Chandrasekar-Fermi and the Structure Function methods.

4.2 Davis-Chandrasekar-Fermi method

The magnetic field strength in the plane-of-the-sky component can be estimated by applying the Davis-Chandrasekhar-Fermi (DCF) method (Davis & Greenstein 1951; Chandrasekhar & Fermi 1953). Under the action of turbulence, an ordered magnetic field will be disturbed and will show scatter in the linear polarization vectors. Given the volume gas density ρ, the angular dispersion of the local magnetic field orientation σ_ψ and the one-dimensional velocity dispersion of the gas σ_ν, the strength of the magnetic field component in the plane of the sky in Gauss is

$$B_\perp^{\mathrm{DCF}} = \xi\sqrt{4\pi\rho}\frac{\sigma_\nu}{\sigma_\psi} \tag{4.1}$$

where we assume that the magnetic field is frozen in the medium and σ_ψ and σ_ν are both caused by turbulent motions. In this case the turbulence is isotropic and incompressible, and the turbulent magnetic energy is small compared to the mean-field magnetic energy. In Eq. (4.1), $\rho = \mu n m_H$ is in g cm^{-3} (where μ is the molecular weight in atomic units, n the density in cm^{-3}, and m_H the hydrogen mass), σ_ν is cm s^{-1} and σ_ψ is in rad.
Other assumptions are the presence of a mean magnetic field in the region and the dispersion of σ_ψ is due to transverse and incompressible Alfvén waves. Since this method was developed to infer the magnetic field strength in the diffuse ISM, a correction factor ξ has been introduced and it is usually taken as $0.3 \leq \xi \leq 0.5$ from simulations of MHD turbulence in molecular clouds (Ostriker et al. 2001; Padoan et al. 2001; Heitsch et al. 2001; Falceta-Gonçalves et al. 2008). To avoid an overestimate of $B_\perp^{\mathrm{DCF}}$, ξ must be applied in the case of strong magnetic field (i.e. $\sigma_\psi \leq 25°$).
However, Crutcher et al. (2003) argued that self-gravitating cores were not properly resolved in those simulations, since the simulations were halted after the formation of dense filaments because of insufficient resolution to follow the evolution further. Moreover, Cho & Yoo (2016) pointed out that in the presence of averaging (e.g. on σ_ψ along the line of sight or on the polarization angle within the telescope beam), the DCF method overestimates the magnetic field strength and thus a correction factor $0.7 \leq \xi \leq 1.0$ must be introduced.
The angular dispersion of the local magnetic field orientation can be estimated over selected pixels in each POLI images, considering

$$\sigma_\psi = \sqrt{\langle(\Delta\psi)^2\rangle} \tag{4.2}$$

$$\Delta\psi = 0.5 \times \arctan\left(\frac{Q\langle U\rangle - \langle Q\rangle U}{Q\langle Q\rangle - \langle U\rangle U}\right) \tag{4.3}$$

where ψ is the polarization orientation angle and $\langle ...\rangle$ denotes an average over the selected pixels in each map (Planck Collaboration et al. 2016, 2015).

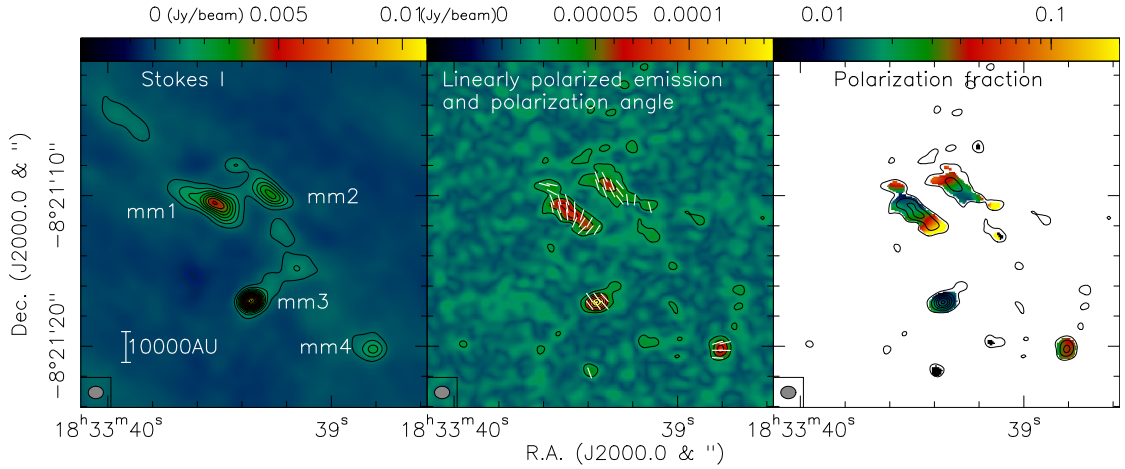

Figure 4.2: ALMA 1.3 mm continuum observations of IRDC18310-4 (Beuther et al. 2018). In the left panel is given the Stokes I emission (4σ contours of 0.6 mJy beam^{-1}), and in the middle panel the linearly polarized emission (4σ contours of 24 μJy beam^{-1}). The line segments indicates the polarization angles. The right panel shows the polarization fraction overplotted the same contours of linearly polarized emission as in the middle panel.

The velocity dispersion $\sigma_\nu \sim \Delta\nu/\sqrt{8\ln 2}$ can be estimated from spectral lines observed in the same regions.

However, the magnetic field values inferred with the DCF method should be considered as order-of-magnitude estimates because they do not fully cover the complexity of the field dynamics inside the protostar. For example, the value of σ_ψ is an average of magnetic field vectors and it is complicated to determine the area in which this average must be obtained, especially in sources showing complicated structures such as filaments. Moreover another source of uncertainty in the DCF method is given by the choice of turbulent velocity because it is not clear which molecular line offers the best tracer for the dust turbulent velocity. In addition, the magnetic field structure inside a star forming region can be affected by effects that are not accounted in the DCF analysis, such as differential rotation, gravitational collapse, or expanding HII regions. Therefore, a distortion in polarization position angles can be observed because of large-scale non-turbulent effects. Consequently, the dispersion values inferred from the mean fields can be much larger than what should be attributed to MHD waves or turbulence (Hildebrand et al. 2009; Houde et al. 2009).

Therefore, various statistical methods have been developed in order to avoid some of the DCF method shortcomings (Hildebrand et al. 2009; Houde et al. 2009; Koch et al. 2010). The structure function (SF) of the polarization angles is a possible way to overcome the problem of underestimating $B_\perp^{\rm DCF}$.

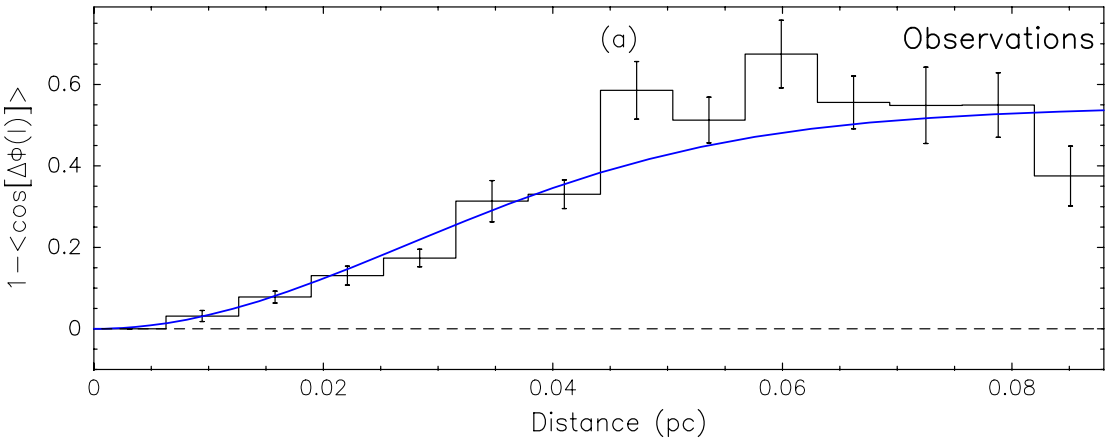

Figure 4.3: Structure function of the polarization angles, towards NGC 6364 V as in Fig. 4.1. The solid black line and error bars are the mean and standard deviation of all the pairs contained in each bin. The blue line shows the fit to the data using a core size δ of 25 mpc. Figure adapted from Juárez et al. (2017).

4.3 Structure function

The structure function is also known as dispersion function of the polarization orientation angles and gives an estimate of the mean square deviation of the magnetic field $B_\perp$ as a function of the scale size. It consists of computing the mean absolute difference between polarization angles as a function of their displacement l, considering a polarization emission perpendicular to magnetic field. Large values of the SF imply large variations, while small values indicate a small dispersion between measured polarization angles. Two examples of SF are given in Fig. 4.3 and Fig. 4.4 obtained from the analysis of NGC 6364 V (Juárez et al. 2017) and IRDC 18310-4 (Beuther et al. 2018) seen in Chapter 4.
The advantages of this method are that the SF does not depend on any model of the large-scale magnetic field and can be used to infer the turbulence to large-scale magnetic field strength ratio. However, it can only be applied under the same conditions as the DCF method, i.e. a smooth low-noise polarization image, well-known densities, and moderately uniform gas velocities.
The magnetic field dispersion $S(l)$ corresponds to the square root of the SF of the polarization orientation angles towards each source and is defined as

$$S^2(l) = b^2 + m^2 l^2 + \sigma_M^2(l), \tag{4.4}$$

where b gives the turbulent contribution to the angular dispersion, m^2 is a constant, and $\sigma_M^2(l)$ represents the uncertainty on the polarization angles (Hildebrand et al. 2009; Houde et al. 2009; Koch et al. 2010). The magnetic field is composed by a large-structure field B_0 and by a random component B_t and their relationship is

given by

$$\frac{B_t}{B_0} = \frac{b}{\sqrt{(2-b^2)}} \quad . \tag{4.5}$$

If this ratio is less than one, then the large-scale magnetic field dominates over the turbulent component. Considering the same assumptions of the DCF method, i.e. incompressible and isotropic turbulence, magnetic field frozen into the gas, and dispersion of the $B_\perp$ orientation originating in transverse incompressible Alfvén waves,

$$\frac{B_t}{B_0} = \frac{\sigma_\nu}{\sigma_A} \quad , \tag{4.6}$$

where $\sigma_A = B_0(4\pi\rho)^{-\frac{1}{2}}$ is the Alfvén velocity.
The magnetic field component on the plane of the sky computed using the SF method can be obtained combining Eq. (4.5) and Eq. (4.6):

$$B_\perp^{\rm SF} = \sqrt{4\pi\rho}\frac{\sigma_\nu\sqrt{2-b^2}}{b} \quad . \tag{4.7}$$

When $B_t \ll B_0$, then Eq. (4.7) can be approximated

$$B_\perp^{\rm SF} \simeq \sqrt{8\pi\rho}\frac{\sigma_\nu}{b} \quad . \tag{4.8}$$

By fitting $S^2(l)$, we can derive the intercept of the fit b^2, and its square root gives an alternative measure for the dispersion of polarization angles σ_ψ.
In case of low resolution data, it can be necessary to apply a beam correction $\sim \sqrt{N}$ to avoid an underestimate of the B_t/B_0 ratio (Houde et al. 2009; Koch et al. 2010), considering the number of turbulent cells $N \sim$2 given by

$$N = \frac{(\delta^2 + 2W^2)\Delta'}{\sqrt{2\pi}\delta^3} \tag{4.9}$$

where W is beam radius, Δ' is the effective depth of the molecular cloud along the line of sight, and δ is the turbulent correlation length.

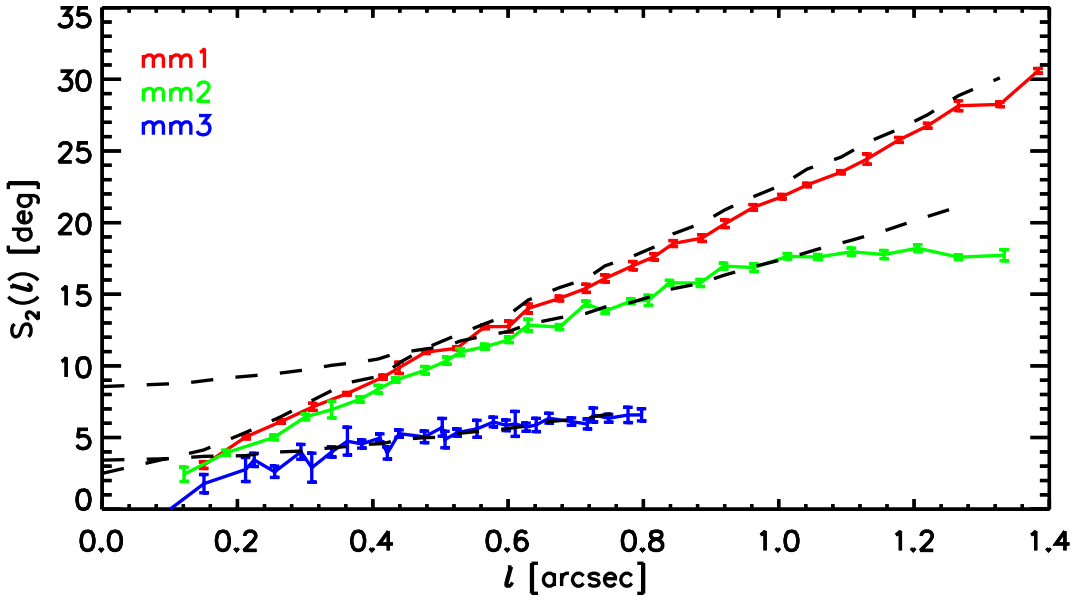

Figure 4.4: Structure function of the polarization angles, towards each cores of IRDC18310-4 as in Fig. 4.2. The dashed lines correspond to the fit to the values of SF in the range $1 \geq 0.4''$ (Beuther et al. 2018).

Chapter 5

Instruments and observations

High angular resolution observations performed by radio interferometers are crucial to study star forming regions, and in particular massive protostars that are usually formed in dense cluster. As mentioned in Chapter 2, to understand how the magnetic fields act on the formation of new stars, it is essential to have a wide view, covering from large to small scales. Large scale surveys in the IR or sub-mm range performed with satellite telescopes such IRAS, Herschel, Plank or Spitzer already identified several high-mass star formation candidates, but with a limited resolution of 1-10″. Interferometers provide the high resolution and high sensitivity necessary to thoroughly investigate these regions, from parsec-scale filament to core-size of few astronomical units. In Fig. 5.1, we give some cases of angular resolution achieved. For example, considering a range of resolution spanning from 0.01″ to 1″, it is possible to resolve structure from clump to disc sizes (10000-10 au) at a distance of 1-10 Kpc. Thus, outflows and cores can be resolved with great accuracy, allowing for chemical and dynamical studies from the outer regions of the prestellar envelope to the inner part of the accretion disc. In these regions masers usually show up with several features and each of them has typically a very small angular extent. Thus high angular resolution imaging is also fundamental to separate and identify each maser spot, allowing for astrometric measurements and for comparison of masers from different molecular species. In addition, masers commonly present strong and narrow spectral lines, and therefore the best way to observe them is to use an instrument offering spectral windows with a large amount of narrow frequency channels and very long baselines. Many modern interferometers have been providing these capabilities and have been revealing the deeply embedded regions of molecular clouds, covering frequencies from centimetre to sub-millimetre. Some of them are the Very Long Baseline Array (VLBA), the Submillimeter Array (SMA), the Jansky Very Large Array (JVLA), the Northern Extended Millimeter Array (NOEMA), Submillimeter Array (SMA), the Australia Telescope Compact Array (ATCA), the Korean VLBI Network (KVN), and last

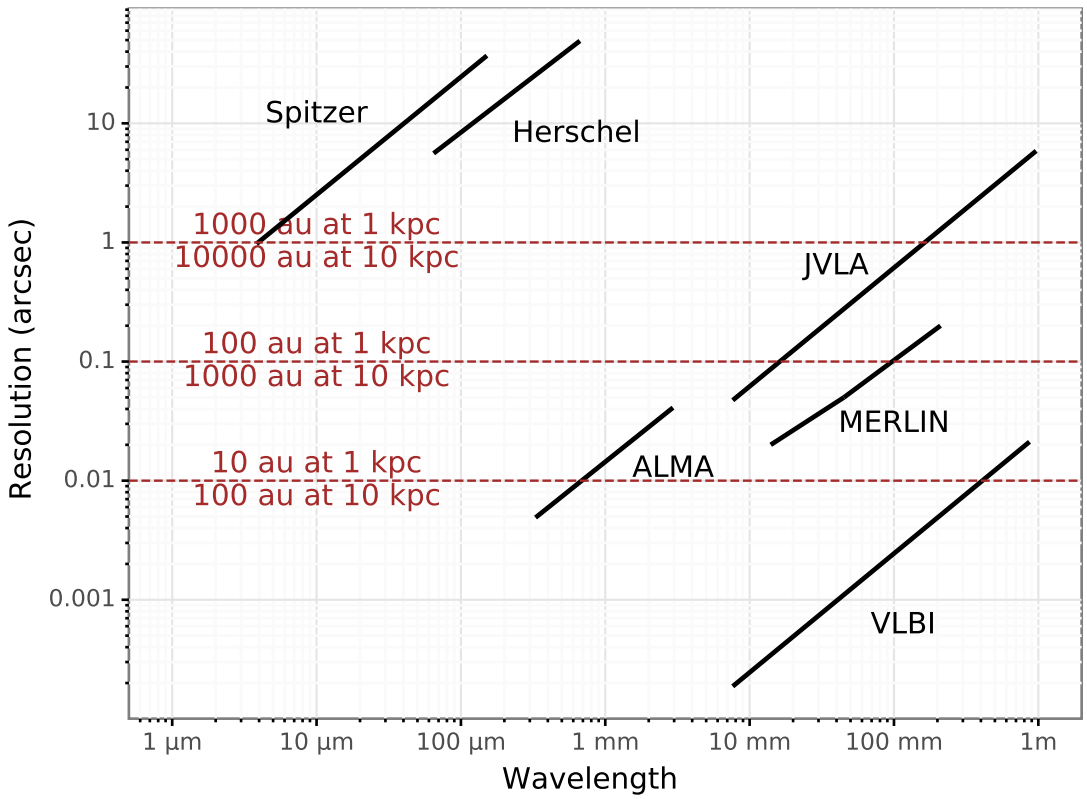

Figure 5.1: Angular resolution achieved for several interferometers and satellites. Given a range of resolution spanning from $0.01''$ to $1''$, it is possible to resolve structures from clump to disc sizes (10000-10 au) at a distance of 1-10 Kpc. Here with VLBI we consider all the network that uses the Very Long Baseline Interferometry technique. Figure adapted from Hirota (2018).

not least the Multi-Element Radio Linked Interferometer Network (MERLIN) and the Atacama Large Millimetre/submillimetre Array (ALMA), that were used in this thesis work.

5.1 MERLIN

MERLIN is an array of seven radio telescopes distributed across the UK, with a maximum baseline of 217 km. The antennas are connected to a central correlator located at the Jodrell Bank Observatory (JBO) and operated as a radio-interferometer. In Paper I we made use of data coming from MERLIN that observed IRAS 18089-1732 at 6.7 GHz, in March, April, and July 2008. The data reduction was carried out using the Astronomical Image Processing Software (AIPS version DEC 2016).
MERLIN has now been updated to e-MERLIN. The enhancements are focused to improve precision astrometry of water, hydroxyl and methanol masers to probe magnetic fields and kinematics in star-forming regions with extraordinary accuracy. The improvements should include wider bandwidth, allowing for multi-line spectroscopy with simultaneous observations of the continuum. This is important to compare the region where the masers arise with the associated continuum, and see if there are interesting characteristic influencing the environment. Large bandwidth gives also the advantage of a large field of view necessary for mapping and wide survey projects.

5.2 ALMA

ALMA is a reconfigurable interferometer composed of 66 high-precision antennas. ALMA consists of two arrays, a larger one called "the 12-m array" and a more compact one named Atacama Compact Array (ACA). The bigger one is composed of 50 movable antennas with 12 m diameter dishes, offering a maximum baseline of up to 16 km in the extended configuration and of 150 m in the compact assembly. The ACA counts 16 fixed antennas closely packed together, covering baselines between 9 and 32 m. The 12 antennas are 7 m diameter dishes while the remaining 4 are 12 m diameter dishes. Thanks to ACA, the sensitivity of ALMA to extended sources and low brightness objects is drastically enhanced. ALMA is located on the Chajnantor plain, a part of the Atacama Desert, in the Chilean Andes at an elevation of about 5000 m. The Atacama Desert is known as one of the driest places on Earth and that makes it one of the best locations to conduct astronomical mm/sub-mm observations, thanks to the absence of cloud cover and water vapour. In addition to its high elevation, it also has the advantage of being free from light pollution and radio interferences by human activities.
In Paper II we made use of band 7 (1 mm) ALMA data to study the source

G9.62+0.20. The observations were performed using 39 antennas of the ALMA 12-m array in May 2015 and 42 antennas in June 2015. Two different array configurations were used (C36-3, C36-4) with baselines range between 17 and 630 m in May and between 15 and 850 m in June. The datasets were reduced using the Common Astronomy Software Application package (CASA version 4.6.0), and the calibration was performed following the procedures provided by the ALMA observatory.

Chapter 6

Introduction to the appended papers

In this chapter a summary is presented of the results of our works, together with an outlook of future perspectives and follow up analysis.

6.1 Paper I

By analysing our MERLIN data, we identified 9 masers in March and April and 7 masers in July 2008, confirming almost all the maser features already seen in previous works and presenting some new detections. In Table 6.1 I report all the maser features observed in March and plotted in Fig. 6.1 (for the April and July detections see the attached paper). The average position of maser feature F.01 in the three epochs is $\alpha_{2000} = 18^{\rm h}11^{\rm m}51.398^{\rm s} \pm 0.002^{\rm s}$, $\delta_{2000} = -17°31'29.92'' \pm 0.02''$. In March, the offset of F.01 from its average position is -33 mas in RA and 4.3 mas in Dec. July observations were in dual circular polarization only, so the linear polarization analysis was performed only on the masers observed in the first two epochs, for which we measured the median linear polarization fraction (P_l) and the median linear polarization angle (χ) across the spectrum. We identified two groups of masers on the basis of two different velocities and χ values: a blue group spanning a velocity range from 30.0 to 36.4 km s^{-1}, and a red group from 37.7 to 39.2 km s^{-1}.

The two groups of masers showed ordered linear polarization vectors, and the orientation was preserved in both March and April observations. The blue group had a weighted average angle of $\chi_{B,M} = -24° \pm 8°$ in March and $\chi_{B,A} = -31° \pm 12°$ in April. The red group had only one linearly polarized emission in March with an angle $\chi_{R,M} = -78° \pm 5°$, while in April the weighted polarization angle was $\chi_{R,A} = -70° \pm 2°$.

The brightest features were expected to be close to maxima in all three epochs on the basis of the variability analysis by Goedhart et al. (2009), but for two of the epochs they showed a flux density much lower than predicted by previous works,

Table 6.1: Parameters of the 6.7-GHz methanol maser features detected in IRAS 18089-1732 in March 2008.

(1) Maser	(2) RA offset (mas)	(3) Dec offset (mas)	(4) Peak flux Density(I) (Jy beam^{-1})	(5) $V_{\rm lsr}$ (km s^{-1})	(6) $P_{\rm l}$ (%)	(7) χ ($\circ$)	(8) Δ_{V_L} (km s^{-1})	(9) $P_{\rm V}$ (%)	(10) B$_{los}$ (mG)
F.01	0	0	69.99 ± 0.66	39.24	8.9 ± 1.4	-78 ± 5	–	–	–
F.02	-34.90	14.11	8.53 ± 0.13	38.84	–	–	–	–	–
F.03	43.68	-2.46	5.19 ± 0.06	37.75	–		–	–	–
F.04	28.92	15.60	3.23 ± 0.04	36.43	–	–	–	–	–
F.05	157.26	51.95	4.12 ± 0.05	34.67	–	–	–	–	–
F.06	1098.47	1128.63	40.04 ± 0.40	33.84	3.8 ± 2.7	-50 ± 28	0.4	0.8	5.5 ± 1.7
F.07	54.65	54.52	17.10 ± 0.27	33.53	6.3 ± 0.4	-31 ± 1	–	–	–
F.08	55.04	44.99	6.45 ± 0.07	32.74	9.4 ± 0.3	-16 ± 1	–	–	–
F.09	937.80	1620.90	3.45 ± 0.07	32.70	–	–	–	–	–

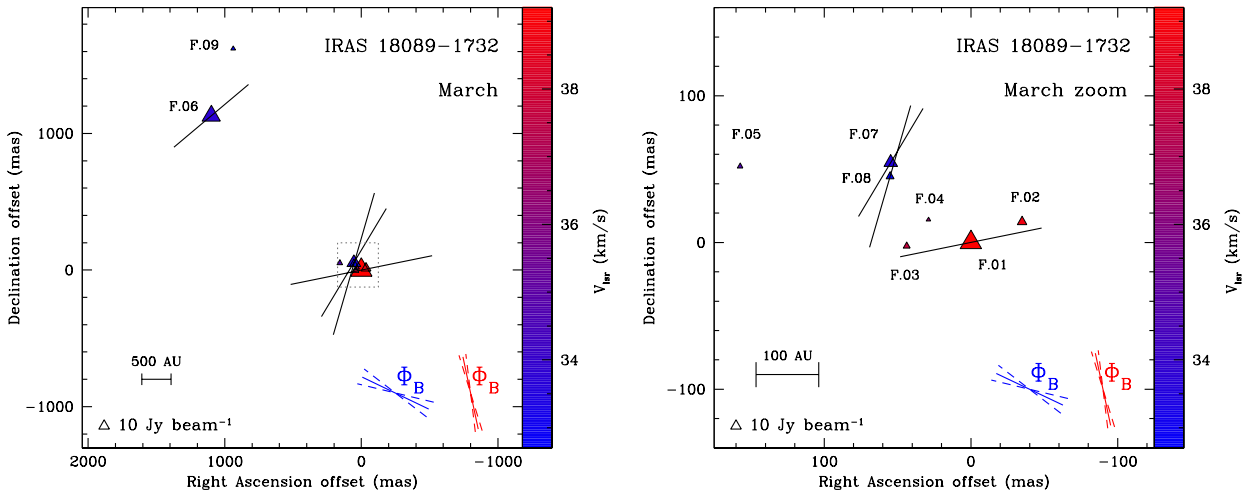

Figure 6.1: Masers identified in March 2008 as listed in Table 6.1. The right panel shows a zoom of the region marked by the dashed grey boxes in the left panel. Each maser is represented by a triangle. The different sizes of the triangles represent the intensity, while the colours indicate the velocity of the maser feature, according to the scale reported in the colour bar. Line segments mark the direction of the polarization vectors for the maser features that show linear polarization. The average direction of the resulting magnetic field Φ_B obtained for the blue and red groups of masers is indicated in the bottom right corners of each panel.

suggesting a change in magnitude or irregular periodicity or both. Our positions, more accurate compared with previous measures, confirmed the separations of features, and suggested lower limits to light travel time, that are in some cases incongruous with the simplest interpretations of time delays.
From the monitoring by Goedhart et al. (2009), we noticed that all the masers in the red group showed variability, with peaks occurring ahead of that of the reference feature, while those in the blue group lag behind. Therefore, since the two groups are separated in polarization angles and velocities, we concluded that the two groups of masers are generated in two different zones, one located on the base of the molecular outflow and another one laying on the disc of the protostar. Consequently, we suggest they are probing two different magnetic field directions, and the resulting orientation on the plane of the sky of $\Phi^{disc} = +62^{\circ} \pm 3^{\circ}$ and $\Phi^{outflow} = +14^{\circ} \pm 4^{\circ}$.
We showed that the small-scale magnetic field probed by the masers is consistent with the large-scale magnetic field traced by the dust (see Fig. 6.2 where we overplotted polarized dust emission from Beuther et al. 2010 and my results).
Therefore we conclude that the large scale field component (traced by dust), prevails over any small scale field fluctuations (traced by masers).
For one of the brightest features, we proposed a tentative detection of circular polarization. Between March and April, the spectral profiles of the total power and of the circular polarization appear to invert. We presented three possible explanations. The reversal could be caused by the splitting of two hyperfine components, each one emitting preferentially in a different epoch. The second possibility could be that the magnetic field inverted its sign. Finally it could be attributable to two different masers, originated in two distinct places but lying along the same line of sight. For all the options, we obtained a $|B_{los}| \sim 5$ mG, comparable to $B_{pos} \sim 11$ mG already obtained by Beuther et al. (2010) for dust.

6.1.1 Follow-up work

New insights on the topic discussed in this paper might come from increasing the number of cases in which line polarization is observed. For example, one could aim at detecting the Goldreich-Kylafis effect in more cases, by inspecting for example the thermal molecular emission coming from the different shells of hot cores. Interferometers such ALMA provide enough sensitivity to enable this kind of study. We obtained ALMA observations in band 6 and band 7 of IRAS 18089-1732 aimed to detect the Goldreich-Kylafis effect. We plan to analyse polarized spectra to obtain information about the strength and the morphology of the magnetic field coming from various environments and tracing different densities and optical depths. Comparing the results with the data already obtained from polarized dust observations and methanol masers, we will derive a 3D structure of the magnetic field and a multi-wavelength and multi-scale view of the magnetic field using three

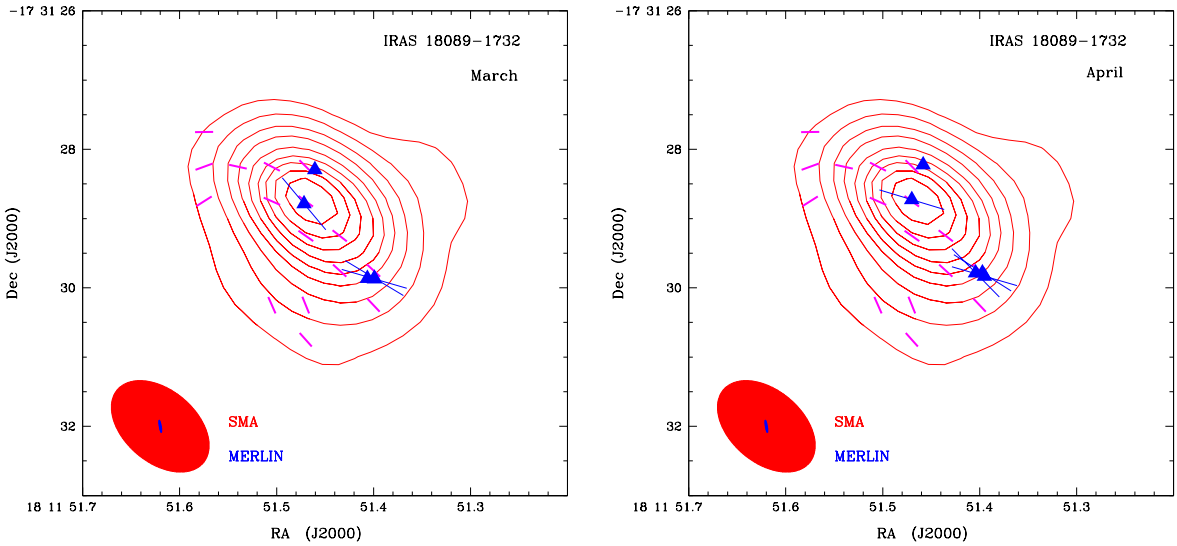

Figure 6.2: Masers in the blue group (blue triangles and blue segments) superimposed on the integrated I image of the dust continuum emission observed by Beuther et al. (2010) at 880 μm with SMA (red contours; the contours are drawn in 10σ steps). The magenta line segments show the magnetic field orientation obtained by linearly polarized dust emission (Beuther et al. 2010). The blue segments represent the magnetic field orientation obtained by our linearly polarized methanol maser emission; it is consistent in March (left panel) and April (right panel) therefore the magnetic field follows the same direction indicated by the dust emission. The red and blue ellipses show the beams of SMA (1.65″ × 1.05″, position angle 51°) and MERLIN, respectively.

different and independent methods.

6.2 Paper II

In this paper we investigated the magnetic field properties at the initial stages of massive star formation and the processes related to the fragmentation and collapse and how they are linked to magnetic fields.
G9.62+0.19 is a well known high-mass star forming region presenting several cores at different evolutionary stages. We made use of ALMA observations in full polarization mode at 1 mm wavelength (Band 7) and analysed the polarized dust emission. We resolved several protostellar cores embedded in a bright and dusty filamentary structure as shown in Fig. 6.3. We identified 23 cores and substructures and we reported the position, the peak flux densities, the integrated flux, the deconvolved major and minor axes, position angles and spectral index (see Tab. 6.2).

Table 6.2: Parameters of the continuum sources of the 1mm ALMA observations of G9.62+0.19.

core		RA Offset ($''$)	Dec Offset ($''$)	I_{Peak} (mJy/beam)	Integrated flux (mJy)	a (milliarcsec)	b (milliarcsec)	P.A. $\circ$	α	β	N(H_2) cm^{-2}	Mass $M_\odot$	λ
MM1a		-4.58 ± 0.04	7.56 ± 0.02	24.5 ± 2.7	114.0 ± 13.0	726 ± 4	426 ± 7	110.6 ± 9.6	3.4 ± 0.5	1.6	2.9×10^{24}	10	—
MM1b		-3.93 ± 0.05	6.75 ± 0.02	21.4 ± 2.7	98.0 ± 12.0	712 ± 2	432 ± 3	90 ± 12	—	—	—	—	—
MM2		-4.06 ± 0.00	4.46 ± 0.00	11.0 ± 0.0	19.2 ± 0.0	374 ± 13	138 ± 42	117 ± 16	—	—	—	—	—
MM3a		-0.20 ± 0.00	5.06 ± 0.00	27.6 ± 2.0	221.0 ± 18.0	1251 ± 105	419 ± 47	0.06 ± 0.02	3.3 ± 0.3	1.5	3.5×10^{24}	21	8
MM3b		-0.25 ± 0.00	4.02 ± 0.00	23.0 ± 2.7	54.4 ± 8.8	384 ± 69	281 ± 93	1.16 ± 0.68	—	—	—	—	—
MM4a	E	-1.53 ± 0.00	3.35 ± 0.00	321.6 ± 6.8	699.0 ± 20.0	402 ± 18	238 ± 15	58.4 ± 4.5	3.8 ± 0.2	1.8	9.5×10^{24}	43	6
MM4b	E	-1.84 ± 0.03	3.25 ± 0.02	82.6 ± 5.3	508.0 ± 37.0	1162 ± 94	345 ± 34	119.4 ± 2.1	—	—	—	—	—
MM5		-1.19 ± 0.02	2.20 ± 0.01	43.1 ± 6.2	42.4 ± 6.1	—	—	—	—	—	—	—	—
MM6a		-0.04 ± 0.00	0.13 ± 0.00	65.6 ± 1.9	64.6 ± 1.8	—	—	—	—	—	—	—	—
MM6b		0.40 ± 0.02	-0.37 ± 0.02	14.8 ± 1.9	14.6 ± 1.8	—	—	—	—	—	—	—	—
MM6c		0.06 ± 0.01	-0.01 ± 0.02	42.6 ± 1.6	251.0 ± 11.0	1057 ± 50	324 ± 24	167.3 ± 1.5	3.9 ± 0.3	2.1	5.8×10^{24}	22	—
MM7	G	0.30 ± 0.01	-2.30 ± 0.01	168.9 ± 11.0	321.0 ± 30.0	359 ± 45	152 ± 82	175 ± 15	3.8 ± 0.5	1.8	3.5×10^{25}	15	—
MM8a	F	1.32 ± 0.00	-4.52 ± 0.00	366.7 ± 7.5	675.0 ± 20.0	342 ± 17	210 ± 11	85.2 ± 4.1	3.8 ± 0.3	1.8	4.7×10^{25}	38	21
MM8b	F	1.15 ± 0.02	-4.73 ± 0.04	80.7 ± 4.8	1011.0 ± 65.0	1612 ± 107	568 ± 44	7.2 ± 2.2	—	—	—	—	—
MM8c	F	1.25 ± 0.03	-3.75 ± 0.01	44.6 ± 6.9	43.9 ± 6.8	—	—	—	—	—	—	—	—
MM9		3.51 ± 0.03	-6.43 ± 0.02	63.4 ± 7.6	147.0 ± 17.0	364 ± 0	310 ± 0	87.8 ± 0.1	3.1 ± 0.7	1.3	1.9×10^{25}	23	—
MM10		2.18 ± 0.04	-6.61 ± 0.03	23.0 ± 4.1	53.4 ± 9.6	402 ± 34	259 ± 47	36 ± 36	—	—	—	—	—
MM11a	D	2.03 ± 0.01	-8.26 ± 0.03	42.8 ± 2.1	277.0 ± 15.0	1046 ± 62	363 ± 32	172.1 ± 2.1	2.7 ± 0.4	0.9	8.7×10^{24}	37	—
MM11b	D	2.30 ± 0.02	-8.19 ± 0.01	20.3 ± 2.4	20.0 ± 2.4	—	—	—	—	—	—	—	—
MM11c	D	1.91 ± 0.01	-8.78 ± 0.02	17.3 ± 2.4	17.1 ± 2.4	—	—	—	—	—	—	—	—
MM12a		3.20 ± 0.03	-10.81 ± 0.03	6.8 ± 1.4	8.7 ± 1.8	—	—	—	—	—	—	—	—
MM12b		3.42 ± 0.03	-11.38 ± 0.04	6.2 ± 1.4	8.3 ± 1.9	—	—	—	—	—	—	—	—
MM12c		3.68 ± 0.03	-12.16 ± 0.03	7.3 ± 1.4	10.3 ± 2.0	—	—	—	—	—	—	—	—

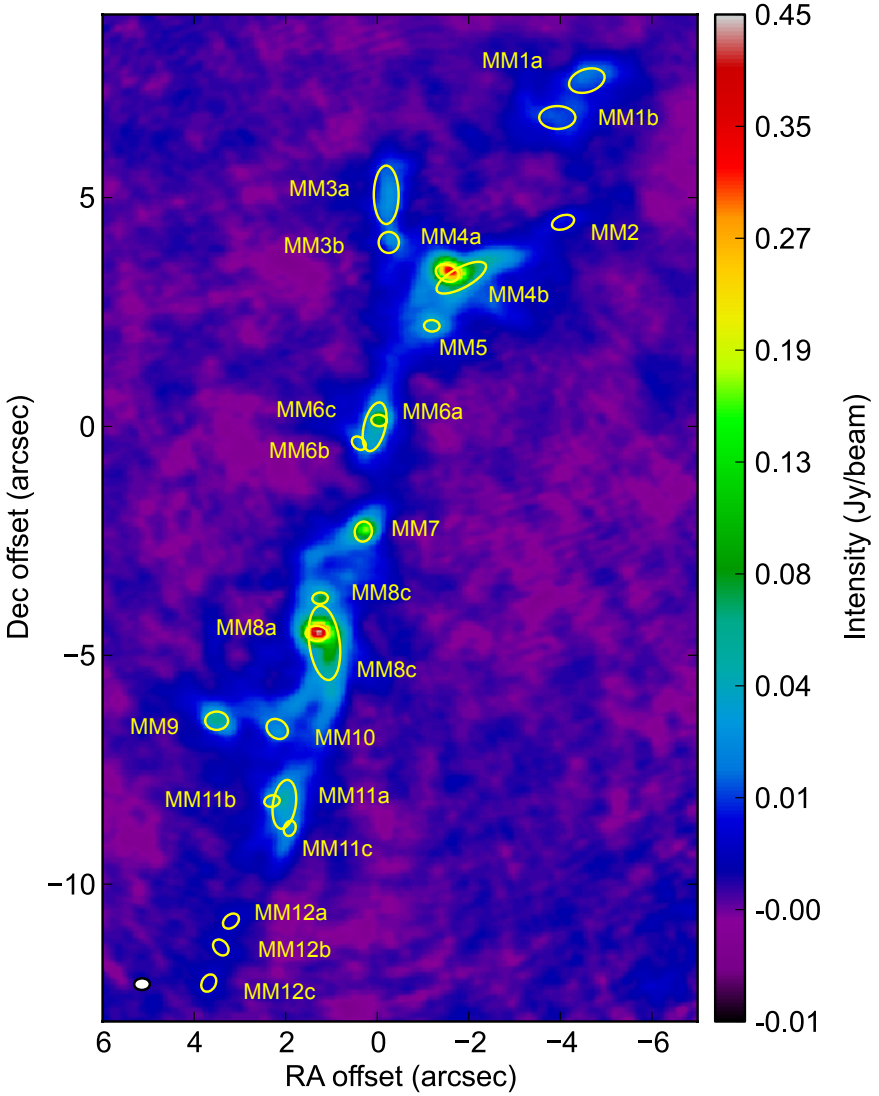

Figure 6.3: Total intensity image of the star forming region G9.62+0.19, with the identified cores. The offsets are relative to the absolute position $\alpha_{2000} = 18^{\rm h}06^{\rm m}14.78000^{\rm s}$, $\delta_{2000} = -20°31'34.90''$. The white ellipse represents the beam and the yellow ellipses represent the dense cores identified by the Gaussian fit and illustrated in Tab. 6.2. The colour scale goes from -0.01 to 0.45 Jy beam $^{-1}$.

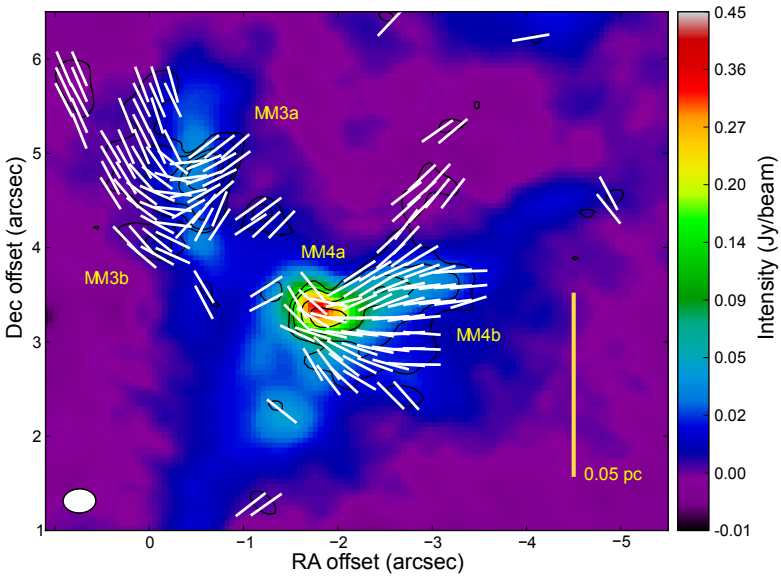

Figure 6.4: Zoom on the cores MM3 and MM4, with the relative sub-cores. The contours represent linearly polarized emission and the levels are (0.3, 0.5, 1.0, 1.5, 2.0) mJy beam^{-1}. The segments indicate linear polarization vectors already rotated of 90° to show the orientation of the magnetic field. In the figure the sampling of the vectors are every 165 by 165 mas. The offsets are relative to the same position as in Fig. 6.3 and the colour scale indicates the total intensity of the background image in Jy beam $^{-1}$, going from -0.01 to 0.45 Jy beam $^{-1}$; the yellow bar indicates the physical scale of 0.05 pc, at the distance of the source.

The linearly polarized emission is clearly detected in six cores, two in the northern field and four in the southern field. (Fig. 6.4 and Fig. 6.5).
One of them, MM3a presents a linear polarization fraction of $\sim 10\%$. For all these cores we studied the magnetic field strength on the plane of the sky component $B_{\perp}$, comparing the Davis-Chandrasekhar-Fermi (DCF) and the Structure Function (SF) methods (see Tab. 6.3).
The estimates of the magnetic field strength along the line of sight derived through the SF method resulted to be larger than the values obtained by the DCF method. By comparison with band 6 observations (Liu et al. 2017), for some of the cores we obtained the spectral index and estimated the N(H_2) column densities and the masses. Due to the large uncertainties on the spectral index and on the optical depth, mainly influenced by the errors on the dust model, the errors on the masses and column densities are arduous to quantify and could be more than a factor of 5. We found that the core masses vary roughly between 10 and 40 $M_{\odot}$ and the N(H_2) column densities between 3×10^{24} and 5×10^{25} cm^2.
Overall the magnetic field is oriented along the filament and appears perpendicular to the direction of the outflows emitted by massive protostellar cores such as

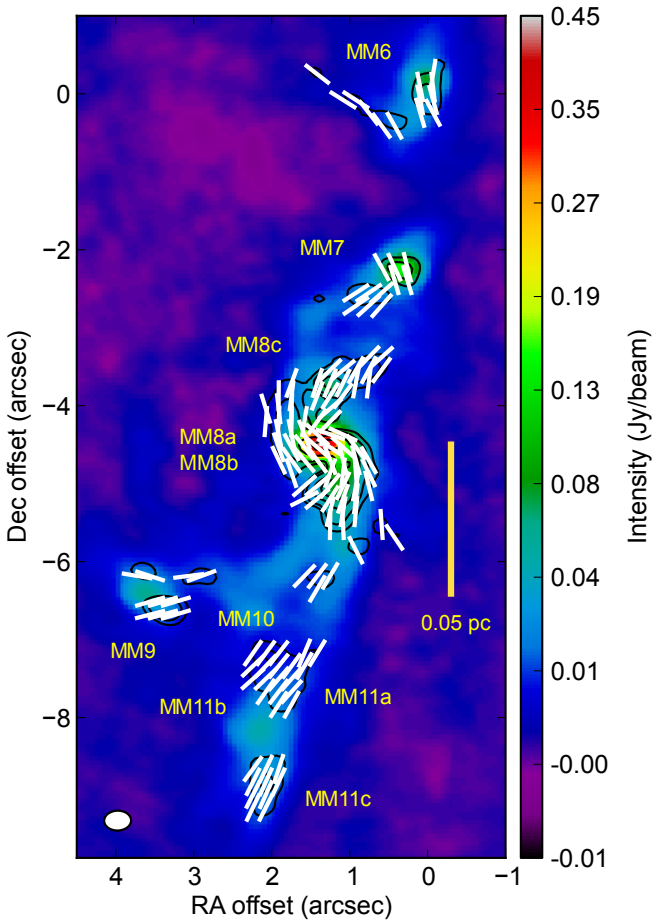

Figure 6.5: Zoom on the core MM8 and relative sub-cores. Contours, colour scale and vectors as in Fig. 6.4

Table 6.3: Polarized intensities and magnetic field parameters.

Core	I_{peak} (mJy beam^{-1})	I_{pol} (mJy beam^{-1})	σ_ψ (°)	σ_v (km s^{-1})	$B_\perp^{DCF}$ (mG)	b (°)	$B_\perp^{SF}$ (mG)	B_t/B_0
MM3	27.6	2.79±0.07	41.8 ± 0.1	2.00 ± 0.01	0.33 ±0.02	11.9 ± 0.2	3.30 ±0.07	0.2
MM4	321.6	1.80±0.06	28.0 ± 0.4	2.00 ± 0.01	1.57 ±0.02	9.4 ± 0.3	13.18 ±0.42	0.1
MM7	168.9	0.66±0.08	—	—	—	—	—	—
MM8a	366.7	1.74±0.08	30.5 ± 3.8	2.35 ± 0.01	1.64 ±0.02	8.6 ± 0.4	17.10 ±0.75	0.1
MM8c	44.6	1.25±0.08	—	—	—	—	—	—
MM9	63.4	0.91±0.07	—	—	—	—	—	—
MM11a	42.8	0.54±0.10	—	—	—	—	—	—

MM8a, MM7 and MM6. At scales less than 0.1 pc, the polarization vectors present ordered patterns and the cores exhibiting polarization are less fragmented than the ones not showing polarized emission. We proposed an evolutionary sequence of the magnetic field of the two hot cores MM4 and MM8. The less evolved hot core MM8 exhibits a magnetic field stronger than MM4, the more evolved one. MM3 is a starless core at the onset of its formation without signature of collapse.
We also observed linearly polarized molecular lines, thermally emitted probably by methanol or carbon dioxide. Moreover, from the Structure Function analysis we measured an average magnetic field strength of the order of 11 mG.
The magnetic field strength along the line of sight, already detected from previous OH and CH_3OH masers observations of cores MM4b and MM7 (Fish et al. 2005; Vlemmings 2008), is comparable with the component on the plane of the sky obtained from our analysis. This could suggest that at scale of less of 0.05 pc the magnetic field role is important in this region.
We measured the ratio of turbulent-to-magnetic energy and we found on average a turbulent-to-magnetic energy ratio of $\gamma \sim 0.07$, suggesting that the magnetic energy along the filament dominates over the turbulent energy.

6.2.1 Follow-up work

Further investigations are needed to properly evaluate the magnetic field strength in the G9.62 region, considering the uncertainties of the DCF and of the SF methods and consequently the errors on column densities and masses. The use of combined observations of masers, dust and molecular lines will contribute in understanding the role of the magnetic field at different scales. More observations of thermal line polarization will add more details and constraints on the magnetic field morphology and strength and will help to infer, for example, a more precise mass-to-magnetic-flux ratio.
Also, in these observations we have shown that the mpc scale field probed by dust continuum emission is consistent with the magnetic field probed by masers (at smaller scales of a few au, observed by VLA). The same consistency between the magnetic field probed by masers and that probed by dust was also found in our work on the massive protostar IRAS18089-1732.
These observations indicate that there is a link between the magnetic fields at different scales, but such a study has been performed only in a few objects and several open questions still need to be addressed. For example, a lack of observations at pc scale in G9.62+0.20 hinders the possibility of carrying out a complete comparison. Moreover, we need to verify if we can expect the same magnetic field evolution in other filaments, and if the magnetic field at pc scale shows also a consistency with that at mpc scales. Therefore, to answer these questions, we proposed ALMA dust polarization observations of Mon R2 hub, a star forming region presenting several cores at different evolutionary stages. Mon R2 has a much more complete

observation coverage then G9.62+20, making it a good target of this study.

6.3 Paper III

Astronomical masers have been effective tools to study magnetic fields for many years. Observations of the linear and circular polarization of different maser species allow to study magnetic fields properties, such as morphology and strength. In particular, methanol is one of the strongest and most common maser observed in massive protostars, and it can probe different regions of protostars such outflows and accretion disc. We explored the polarization properties of some methanol maser transitions, in light of the newly calculated methanol Landé factors (Lankhaar et al. 2016, 2018), and considering hyperfine components.
The maser transitions that we used in our simulations are reported in Tab. 6.4, based on the observations from Breen et al. (2019b), MacLeod et al. (2019), Sarma & Momjian (2020), Momjian & Sarma (2019), Surcis et al. (2019) and Surcis et al. (2009). In the case of the 12.2 GHz maser, we are not modelling a specific source but we are giving a typical value considering the previous work by Moscadelli et al. (2003).
We performed simulations using the radiative transfer code CHAMP (Lankhaar & Vlemmings 2019), for different magnetic field strengths, angular momentum, propagation angles θ, hyperfine components and pumping efficiencies. We compared our results with previous observations and we evaluated the action of preferred hyperfine pumping and non-Zeeman effects on linear and circular polarization.
The linear polarization fraction showed a dependence on the magnetic field strength and on hyperfine transitions. Circular polarization fraction also presented a dependence on the hyperfine transitions.
In Fig. 6.6 and in Fig. 6.7 the linear and circular polarization fraction P_L and P_V are plotted as a function of the maser luminosity for five different θ values. The top left panel, labelled "baseline", indicates a maser emission where all the eight hyperfine transitions contribute equally, while all other panels assume a preferred pumping for the indicated $i \rightarrow j$ transition. The preferred pumping rate is ten times larger than the other transitions' rate. A vertical line marks the locus $g\Omega = 10R$, i.e. where the Zeeman frequency $g\Omega$ becomes much higher than the stimulated emission rate R. When the Zeeman frequency is lower than the rate of stimulated emission, maser emission can be affected by a rotation of the symmetry axis that can intensify or generate circular polarization. Therefore, when $g\Omega < 10R$, inferring magnetic field properties becomes more challenging, because the magnetic field is not directly related to P_L and P_V (Pérez-Sánchez & Vlemmings 2013; Wiebe & Watson 1998).
We also found that distinct hyperfine components react to the magnetic field differently. Thus, in case of preferred hyperfine pumping, high levels of linear and circular polarization can be generated, explaining some of the high P_L and P_V observed and some of the peculiar features seen in the S-shape of observed V-profiles.

Table 6.4: Methanol maser transitions considered in our simulations and observational parameters

Spectral line	Frequency GHz	T_B Lower Limit[a] K	T_B[a] K	Obs. linear pol. %	Obs. circular pol. %	Source and references	code
CH_3OH $17_{-2} \rightarrow 18_{-3}$ E (v_t=1)	6.18	2.2×10^6	5.2×10^{11}	7.0	<0.5	G358.931–0.030[b]	N&W92
CH_3OH $5_1 \rightarrow 6_0$ A^+ (v_t=0)	6.68	7.6×10^6 2.8×10^{13} 1.3×10^{12}	1.5×10^{12} 8.7×10^{13} 6.3×10^{12}	7.5 8.1 4.5	0.5 2.1 0.2	G358.931–0.030[b], W3(OH)[c], W75N[c]	N&W94
CH_3OH $12_4 \rightarrow 13_3$ A^- (v_t=0)	7.68	4.5×10^6	6.5×10^{11}	3.5	<0.5	G358.931–0.030[b]	N&W92
CH_3OH $12_4 \rightarrow 13_3$ A^+ (v_t=0)	7.83	4.5×10^6	6.3×10^{11}	3.5	<0.5	G358.931–0.030[b]	N&W92
CH_3OH $2_0 \rightarrow 3_1$ E (v_t=0)	12.2	$10^9 - 10^{12}$	–	–	–	W3(OH)[d]	N&W94
CH_3OH $17_6 \rightarrow 18_5$ E (v_t=0)	20.3	4.5×10^4	1.7×10^{10}	4.0	2.0	G358.931–0.030[e]	N&W92
CH_3OH $10_1 \rightarrow 11_2$ A^+ (v_t=1)	20.9	3.6×10^4	1.5×10^{11}	7.0	<0.5	G358.931–0.030[b]	N&W92
CH_3OH $5_2 \rightarrow 5_1$ E (v_t=0)	25.0	9.1×10^3	7.2×10^9	–	0.3	OMC–1[f]	N&W94
CH_3OH $4_{-1} \rightarrow 3_0$ E	36.2	1.7×10^1 3.7×10^4	2.6×10^7 3.4×10^9	<0.5 –	<0.5 0.1	G358.931–0.030[b], M8E[g]	N&W94
CH_3OH $7_{-2} \rightarrow 8_{-1}$ E (v_t=0)	37.7	8.7×10^3	1.2×10^{10}	3.5	0.5	G358.931–0.030[b]	N&W92
CH_3OH $7_0 \rightarrow 6_1$ A^+	44.1	1.2×10^2 5.0×10^4	3.15×10^8 1.3×10^{10}	<0.5 –	<0.5 0.05	G358.931–0.030[b], DR21W[h]	N&W94
CH_3OH $2_0 \rightarrow 3_1$ E (v_t=1)	44.9	1.9×10^4	1.7×10^{10}	2.5	<0.5	G358.931–0.030[b]	N&W94
CH_3OH $9_3 \rightarrow 10_2$ E (v_t=0)	45.8	1.4×10^4	1.3×10^{10}	7.0	1.5	G358.931–0.030[b]	N&W92

Notes. [(a)] Brightness temperature is estimated using a maser spot size of 3 mas, while the lower limit is based on the observational details given in the source references. [(b)] From Breen et al. (2019b). [(c)] For W3(OH) we refer to the feature W3OH.22 from Surcis et al. (2019), and for W75N to Surcis et al. (2009). [(d)] We do not model any specific maser but we only report values observed byMoscadelli et al. (2003). [(e)] From MacLeod et al. (2019). [(f)] We used the component 2 of the maser observed by Sarma & Momjian (2020). [(g)] From.Sarma & Momjian (2009). [(h)] We used the component 1 of the maser observed by Momjian & Sarma (2019).

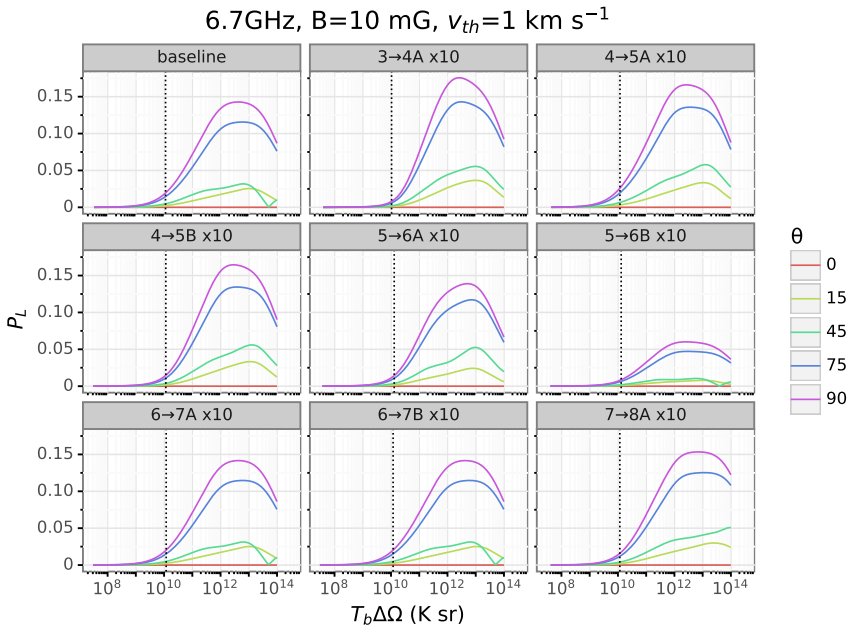

Figure 6.6: 6.7 GHz methanol maser linear polarization fraction as a function of the maser luminosity for five different θ. The vertical line marks $T_B\Delta\Omega$ where $g\Omega = 10R$. The magnetic field strength is 10 mG, the thermal velocity width is 1 km s^{-1}. Preferred hyperfine transitions are given in each panel. The top left panel, labelled "baseline", indicates a fixed pumping rate equal for all the hyperfine transitions, while all others assume a 10× preferred pumping for the indicated $i \rightarrow j$ transition.

We noted the hyperfine splitting of two components for the 6.2 GHz methanol maser, as showed in Fig. 6.8. We see that for v_{th} =1 km s^{-1} the two components are separated and they start to blend for v_{th} =1.25 km s^{-1}. At v_{th} =1.5 km s^{-1} the two hyperfines appear totally blended in one single line. This case explains why it is challenging to detect hyperfine component separation. To observe the hyperfine components it is indeed necessary to have an intrinsic thermal line width that is less than the hyperfine split (v_{th} <1.25 km s^{-1}), otherwise we can only detect one single blended component. However, when the separation is large enough with respect to the intrinsic thermal line width, our simulations predict that multiple components can be observed. Comparison between methanol maser observations and our simulations showed that the rotation of the symmetry axis does not significantly affect methanol masers, but other non-Zeeman contributions need to be taken into account in the study of magnetic fields.

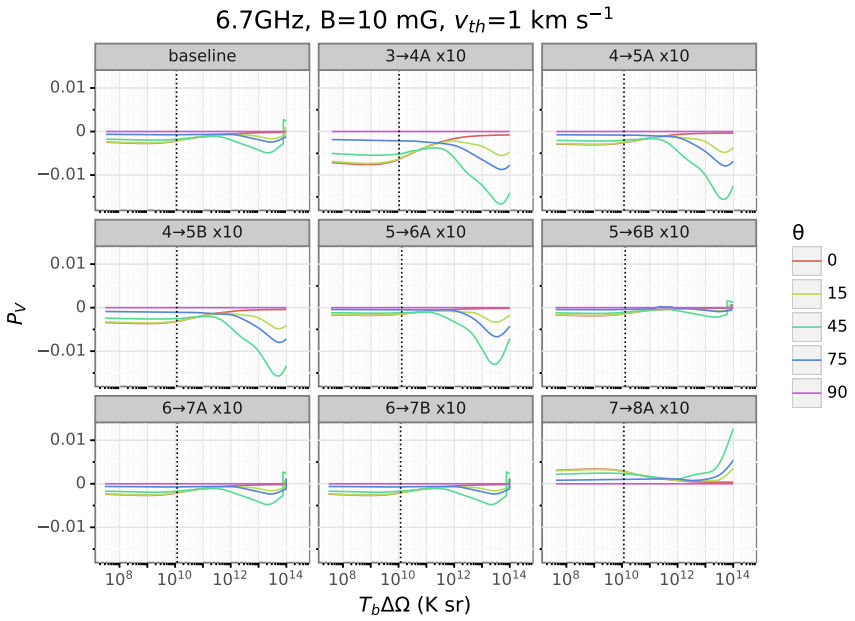

Figure 6.7: 6.7 GHz methanol maser circular polarization fraction as a function of the maser luminosity. Panels as in Fig. 6.6

6.3.1 Follow-up work

Hyperfine preferred pumping plays an important role in modelling linearly and circularly polarized methanol maser emission. Therefore a good way to improve our understanding of the action of hyperfine preferred pumping on polarization is by combining simulations and observations of methanol maser emission at several frequencies. To evaluate the relevance of non-Zeeman effects it is important to obtain good estimates of brightness temperatures and therefore a good knowledge of the maser beaming angles. Moreover by simultaneous observations of P_L and P_V in several maser transitions, it will be possible to rule out the presence of non-Zeeman effects or estimate their real contributions. In order to detect the splitting between the hyperfine components, a splitting width significantly larger than the intrinsic thermal line width is required, as showed by the newly discovered 6.2 GHz masers (Breen et al. 2019b). Therefore, further high angular resolution observations can offer a new insight on methanol masers hyperfine components and will be fundamental for studying the hyperfine splitting.

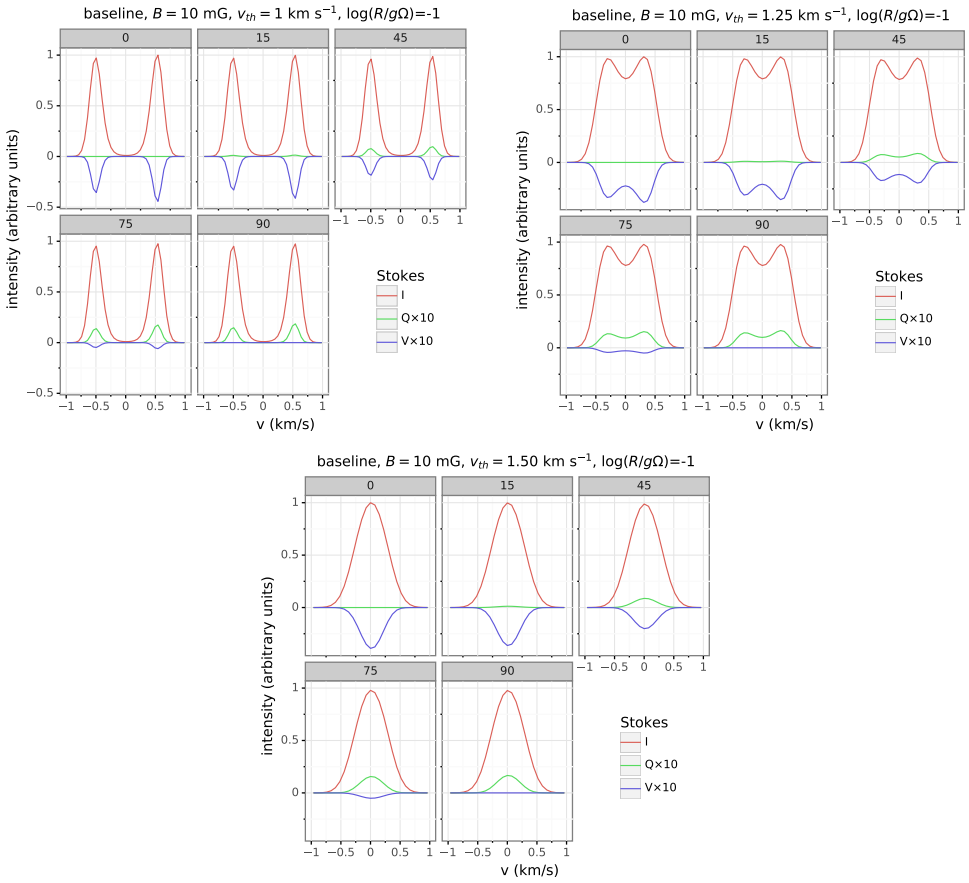

Figure 6.8: Spectra for different intrinsic thermal velocity width for 6.2 GHz methanol maser. Simulations were performed for stokes I, Q, U, and V, and for propagation angles θ of 0, 15, 45, 75 and 90.

Chapter 7

Future prospects

Magnetic fields have been detected only in a limited sample of cases and increasing the number of observed sources is thus crucial to further constrain its role in star formation. Moreover not all evolutionary stages of the star formation process were explored, due to a lack of resolution and sensitivity. Therefore, future surveys should cover several spatial scales from clump size to core scales and should be addressed by taking into account combined observations of masers, dust and molecular lines. Multiwavelength observations indeed could represent a way to inspect the field with independent methods and test its consistency across different physical conditions. This will help for example to determine whether the polarized emission from discs around young forming stars is due to magnetic fields or to other mechanisms such as dust self-scattering (Kataoka et al. 2016, 2017).

Thanks to the resolution and the sensitivity of ALMA, the number of observed massive protostars will increase significantly in the near future. ALMA circular polarization capability will enable milestone studies targeting not just polarized emission from dust but also from molecular lines and it will be possible to detect Zeeman and Goldreich-Kylafis effects. More observations of the Zeeman effects are important to consolidate the relation between magnetic field and density. So, even if recent ALMA observations of the disc of TW Hya (Vlemmings et al. 2019) presented a non detection of the Zeeman effect of CN emission, this result gives an important indication of a possible upper limit of the magnetic field, and it can be used as baseline for further observations to infer more details on the magnetic fields in protostellar disc (Brauer et al. 2017).

We already obtained ALMA data of the massive protostar IRAS 18089-1732 observed in full polarization mode and we will study the Goldreich-Kylafis effect in several molecular species present in this hot core. To properly model the magnetic field inferred from the polarization of these molecular lines, we will use the recently published three-dimensional polarized line adaptive radiative transfer code, PORTAL (Lankhaar & Vlemmings 2020). Comparing these results with our previous

masers and dust observations will give us an unprecedented view of the magnetic field in this source.
To conclude, the next generation of telescopes such as the Next Generation Very Large Array (ngVLA) (Hull et al. 2018) or the Square Kilometre Array (SKA) will offer new improvements in resolution and spectral coverage, offering a new light in observing magnetic fields in deeply embedded source, such as prestellar cores. The ngVLA will operate at longer wavelengths (1 - 116 GHz) and will look at optically thick regions dominated by self-scattering, where ALMA is blind. The high sensitivity of SKA will also offer the chance to detect Zeeman splitting in OH and methanol maser. Thanks to multi-wavelengths and multi-scale observations, covering the full range of evolutionary stages, in the coming years we can expect a vast improvements in our understanding of magnetized star formation.

Useful reviews and books

Finally, in this Chapter I present a list of useful books and comprehensive reviews which I made use of in this work.

Beuther, H., Klessen, R., Dullemond, C., & Henning, T. 2014, Protostars and Planets VI, Space Science Series (University of Arizona Press)

Beuther, H., LInz, H., Henning, T., & of the Pacific, A. S. 2008, Massive Star Formation: Observations Confront Theory : Proceedings of a Conference Held at the Heidelberg Convention Center, Heidelberg, Germany, 10-14 September 2007, Astronomical Society of the Pacific conference series (Astronomical Society of the Pacific)

Bodenheimer, P. 2011, Principles of Star Formation, Astronomy and Astrophysics Library (Springer Berlin Heidelberg)

Bonnell, I. A. & Smith, R. J. 2011, in IAU Symposium, Vol. 270, Computational Star Formation, ed. J. Alves, B. G. Elmegreen, J. M. Girart, & V. Trimble, 57

Braithwaite, J. 2012, MNRAS, 422, 619

Chabrier, G. 2005, in Astrophysics and Space Science Library, Vol. 327, The Initial Mass Function 50 Years Later, ed. E. Corbelli, F. Palla, & H. Zinnecker, 41

Cortes, P. C., Crutcher, R. M., & Watson, W. D. 2005, ApJ, 628, 780

Draine, B. T. 2011, Physics of the Interstellar and Intergalactic Medium (Princeton University Press)

Elitzur, M. 2002, in Astrophysical Spectropolarimetry, ed. J. Trujillo-Bueno, F. Moreno-Insertis, & F. Sánchez, 225–264

Elitzur, M. 2012, Astronomical Masers, Astrophysics and Space Science Library (Springer Netherlands)

Gray, M. 2012, Maser Sources in Astrophysics (Cambridge University Press)

Krumholz, M. R. 2011, in American Institute of Physics Conference Series, Vol. 1386, American Institute of Physics Conference Series, ed. E. Telles, R. Dupke, & D. Lazzaro, 9–57

Krumholz, M. R., Bate, M. R., Arce, H. G., et al. 2014, Protostars and Planets VI, 243

LeBlanc, F. 2010, An Introduction to Stellar Astrophysics (Wiley)

McKee, C. F. & Tan, J. C. 2003, ApJ, 585, 850

Nedoluha, G. E. & Watson, W. D. 1992, ApJ, 384, 185

Reipurth, B. & Schneider, N. 2008, Star Formation and Young Clusters in Cygnus, ed. B. Reipurth, 36

Schulz, N. 2005, From Dust To Stars: Studies of the Formation and Early Evolution of Stars, Springer Praxis Books (Springer Berlin Heidelberg)

Surcis, G., High resolution magnetic field measurements in high-mass star-forming regions, PhD Thesis, University of Bonn, 2011

Tan, J. C., Beltrán, M. T., Caselli, P., et al. 2014, Protostars and Planets VI, 149

Troland, T. H. & Heiles, C. 1982, ApJ, 252, 179

Vlemmings, W. H. T., Circumstellar maser properties through VLBI observations, PhD Thesis, Leiden University, 2002.

Ward-Thompson, D. & Whitworth, A. 2011, An Introduction to Star Formation (Cambridge University Press)

Bibliography

Allen, A., Li, Z.-Y., & Shu, F. H. 2003, ApJ, 599, 363

Alves, F. O., Girart, J. M., Padovani, M., et al. 2018, A&A, 616, A56

Amiri, N., Vlemmings, W. H. T., Kemball, A. J., & van Langevelde, H. J. 2012, A&A, 538, A136

Andersson, B.-G., Lazarian, A., & Vaillancourt, J. E. 2015, ARA&A, 53, 501

Barrett, A. H., Schwartz, P. R., & Waters, J. W. 1971, ApJ, 168, L101

Bartkiewicz, A., Szymczak, M., van Langevelde, H. J., Richards, A. M. S., & Pihlström, Y. M. 2009, A&A, 502, 155

Bayandina, O. S., Val'tts, I. E., & Larionov, G. M. 2012, Astronomy Reports, 56, 553

Beuther, H., Soler, J. D., Vlemmings, W., et al. 2018, A&A, 614, A64

Beuther, H., Vlemmings, W. H. T., Rao, R., & van der Tak, F. F. S. 2010, ApJ, 724, L113

Brauer, R., Wolf, S., & Flock, M. 2017, A&A, 607, A104

Breen, S. L., Contreras, Y., Dawson, J. R., et al. 2019a, MNRAS, 484, 5072

Breen, S. L., Fuller, G. A., Caswell, J. L., et al. 2015, MNRAS, 450, 4109

Breen, S. L., Sobolev, A. M., Kaczmarek, J. F., et al. 2019b, ApJ, 876, L25

Carrasco-González, C., Torrelles, J. M., Cantó, J., et al. 2015, Science, 348, 114

Caswell, J. L. 2004, MNRAS, 349, 99

Caswell, J. L., Fuller, G. A., Green, J. A., et al. 2010, MNRAS, 404, 1029

Caswell, J. L., Kramer, B. H., & Reynolds, J. E. 2011, MNRAS, 414, 1914

Chandrasekhar, S. & Fermi, E. 1953, ApJ, 118, 113

Chibueze, J. O., Csengeri, T., Tatematsu, K., et al. 2017, Proceedings of the International Astronomical Union, 13, 247âĂŞ250

Chibueze, J. O., Csengeri, T., Tatematsu, K., et al. 2017, ApJ, 836, 59

Chibueze, J. O., Imai, H., Tafoya, D., et al. 2012, ApJ, 748, 146

Chibueze, J. O., Nagayama, T., Omodaka, T., et al. 2020, PASJ

Cho, J. & Yoo, H. 2016, ApJ, 821, 21

Compiègne, M., Verstraete, L., Jones, A., et al. 2011, A&A, 525, A103

Crutcher, R. M. & Kemball, A. J. 2019, Frontiers in Astronomy and Space Sciences, 6, 66

Crutcher, R. M., Nutter, D. J., & Ward-Thompson, D. 2003, in Bulletin of the American Astronomical Society, Vol. 35, American Astronomical Society Meeting Abstracts #202, 772

Dall'Olio, D., Vlemmings, W. H. T., Surcis, G., et al. 2017, A&A, 607, A111

Davis, Jr., L. & Greenstein, J. L. 1951, ApJ, 114, 206

de Villiers, H. M., Chrysostomou, A., Thompson, M. A., et al. 2015, MNRAS, 449, 119

Dinh-v-Trung. 2009, MNRAS, 399, 1495

Dodson, R. & Moriarty, C. D. 2012, MNRAS, 421, 2395

Dolginov, A. Z. & Mitrofanov, I. G. 1976, Ap&SS, 43, 291

Draine, B. T. & Fraisse, A. A. 2009, ApJ, 696, 1

Edris, K. A., Fuller, G. A., Etoka, S., & Cohen, R. J. 2017, A&A, 608, A80

Elitzur, M. 1992, Science, 257, 112

Ellingsen, S. P. 2002, in IAU Symposium, Vol. 206, Cosmic Masers: From Proto-Stars to Black Holes, ed. V. Migenes & M. J. Reid, 151

Falceta-Gonçalves, D., Lazarian, A., & Kowal, G. 2008, ApJ, 679, 537

Fiebig, D. & Guesten, R. 1989, A&A, 214, 333

Fish, V. L., Reid, M. J., Argon, A. L., & Zheng, X.-W. 2005, ApJS, 160, 220

Galli, D. & Shu, F. H. 1993a, ApJ, 417, 220

Galli, D. & Shu, F. H. 1993b, ApJ, 417, 243

Girart, J. M., Beltrán, M. T., Zhang, Q., Rao, R., & Estalella, R. 2009, Science, 324, 1408

Girart, J. M., Fernández-López, M., Li, Z.-Y., et al. 2018, ApJ, 856, L27

Girart, J. M., Frau, P., Zhang, Q., et al. 2013, ApJ, 772, 69

Goddi, C., Moscadelli, L., & Sanna, A. 2011, A&A, 535, L8

Goedhart, S., Langa, M. C., Gaylard, M. J., & van der Walt, D. J. 2009, MNRAS, 398, 995

Gold, T. 1952a, Nature, 169, 322

Gold, T. 1952b, MNRAS, 112, 215

Gonçalves, J., Galli, D., & Girart, J. M. 2008, A&A, 490, L39

Gray, M. 2012, Maser Sources in Astrophysics

Green, J. A., Caswell, J. L., & McClure-Griffiths, N. M. 2015, MNRAS, 451, 74

Green, J. A., Richards, A. M. S., Vlemmings, W. H. T., Diamond, P., & Cohen, R. J. 2007, MNRAS, 382, 770

Harvey-Smith, L., Soria-Ruiz, R., Duarte-Cabral, A., & Cohen, R. J. 2008, MNRAS, 384, 719

Heitsch, F., Zweibel, E. G., Mac Low, M.-M., Li, P., & Norman, M. L. 2001, ApJ, 561, 800

Hennebelle, P. & Inutsuka, S.-i. 2019, Frontiers in Astronomy and Space Sciences, 6, 5

Hildebrand, R. H., Kirby, L., Dotson, J. L., Houde, M., & Vaillancourt, J. E. 2009, ApJ, 696, 567

Hirota, T. 2018, Publication of Korean Astronomical Society, 33, 21

Houde, M., Vaillancourt, J. E., Hildebrand, R. H., Chitsazzadeh, S., & Kirby, L. 2009, ApJ, 706, 1504

Hull, C. L. H., Carrasco-González, C., Williams, P. K. G., et al. 2018, in Astronomical Society of the Pacific Conference Series, Vol. 517, Science with a Next Generation Very Large Array, ed. E. Murphy, 357

Hull, C. L. H. & Zhang, Q. 2019, Frontiers in Astronomy and Space Sciences, 6, 3

Ilee, J. D., Cyganowski, C. J., Nazari, P., et al. 2016, MNRAS, 462, 4386

Johansen, A. & Levin, Y. 2008, A&A, 490, 501

Juárez, C., Girart, J. M., Zamora-Avilés, M., et al. 2017, ApJ, 844, 44

Kalenskii, S., Kurtz, S., Hofner, P., et al. 2018, in IAU Symposium, Vol. 336, Astrophysical Masers: Unlocking the Mysteries of the Universe, ed. A. Tarchi, M. J. Reid, & P. Castangia, 33–36

Kataoka, A., Muto, T., Momose, M., et al. 2015, ApJ, 809, 78

Kataoka, A., Tsukagoshi, T., Momose, M., et al. 2016, ApJ, 831, L12

Kataoka, A., Tsukagoshi, T., Pohl, A., et al. 2017, ApJ, 844, L5

Kim, J., Kim, M. K., Hirota, T., et al. 2020, ApJ, 896, 127

Kim, J.-S., Kim, S.-W., Kurayama, T., et al. 2013, ApJ, 767, 86

Klassen, M., Pudritz, R. E., & Kirk, H. 2017, MNRAS, 465, 2254

Koch, P. M., Tang, Y.-W., & Ho, P. T. P. 2010, ApJ, 721, 815

Koch, P. M., Tang, Y.-W., Ho, P. T. P., et al. 2018, ApJ, 855, 39

Koo, B.-C., Williams, D. R. D., Heiles, C., & Backer, D. C. 1988, ApJ, 326, 931

Krasnopolsky, R. & Gammie, C. F. 2005, ApJ, 635, 1126

Krumholz, M. R. & Federrath, C. 2019, Frontiers in Astronomy and Space Sciences, 6, 7

Lankhaar, B., Groenenboom, G. C., & van der Avoird, A. 2016, J. Chem. Phys., 145, 244301

Lankhaar, B. & Vlemmings, W. 2019, A&A, 628, A14

Lankhaar, B. & Vlemmings, W. 2020, A&A, 636, A14

Lankhaar, B., Vlemmings, W., Surcis, G., et al. 2018, Nature Astronomy, 2, 145

Lazarian, A. & Hoang, T. 2007, ApJ, 669, L77

Lekht, E. E., Pashchenko, M. I., & Tolmachev, A. M. 2007, Astronomy Reports, 51, 531

Leurini, S. & Menten, K. M. 2017, Proceedings of the International Astronomical Union, 13, 17âĂŞ22

Leurini, S., Menten, K. M., & Walmsley, C. M. 2016, A&A, 592, A31

Li, H.-B., Yuen, K. H., Otto, F., et al. 2015, Nature, 520, 518

Liu, T., Lacy, J., Li, P. S., et al. 2017, ApJ, 849, 25

MacLeod, G. C., Sugiyama, K., Hunter, T. R., et al. 2019, MNRAS, 489, 3981

Matsumoto, N., Hirota, T., Sugiyama, K., et al. 2014, ApJ, 789, L1

Maury, A. J., Girart, J. M., Zhang, Q., et al. 2018, MNRAS, 477, 2760

Menten, K. M. 1991, in Astronomical Society of the Pacific Conference Series, Vol. 16, Atoms, Ions and Molecules: New Results in Spectral Line Astrophysics, ed. A. D. Haschick & P. T. P. Ho, 119–136

Mestel, L. & Spitzer, L., J. 1956, MNRAS, 116, 503

Minier, V., Burton, M. G., Hill, T., et al. 2005, A&A, 429, 945

Mocz, P., Burkhart, B., Hernquist, L., McKee, C. F., & Springel, V. 2017, ApJ, 838, 40

Momjian, E. & Sarma, A. P. 2017, ApJ, 834, 168

Momjian, E. & Sarma, A. P. 2019, ApJ, 872, 12

Morimoto, M., Ohishi, M., & Kanzawa, T. 1985, ApJ, 288, L11

Moscadelli, L., Cesaroni, R., & Rioja, M. J. 2005, A&A, 438, 889

Moscadelli, L., Menten, K. M., Walmsley, C. M., & Reid, M. J. 2003, ApJ, 583, 776

Moscadelli, L., Sanna, A., & Goddi, C. 2017, Proceedings of the International Astronomical Union, 13, 201âĂŞ206

Moscadelli, L., Sanna, A., Goddi, C., et al. 2020, A&A, 635, A118

Moscadelli, L., Testi, L., Furuya, R. S., et al. 2006, A&A, 446, 985

Mouschovias, T. C. 1976, ApJ, 206, 753

Mouschovias, T. C., Tassis, K., & Kunz, M. W. 2006, ApJ, 646, 1043

Nedoluha, G. E. & Watson, W. D. 1990a, ApJ, 354, 660

Nedoluha, G. E. & Watson, W. D. 1990b, ApJ, 361, 653

Ostriker, E. C., Stone, J. M., & Gammie, C. F. 2001, ApJ, 546, 980

Padoan, P., Goodman, A., Draine, B. T., et al. 2001, ApJ, 559, 1005

Paulson, S. T. & Pandian, J. D. 2020, MNRAS, 492, 1335

Pérez-Sánchez, A. F. & Vlemmings, W. H. T. 2013, A&A, 551, A15

Planck Collaboration, Ade, P. A. R., Aghanim, N., et al. 2015, A&A, 576, A104

Planck Collaboration, Ade, P. A. R., Aghanim, N., et al. 2016, A&A, 586, A138

Pudritz, R. E. & Ray, T. P. 2019, Frontiers in Astronomy and Space Sciences, 6, 54

Qiu, K., Zhang, Q., Menten, K. M., et al. 2014, ApJ, 794, L18

Reid, M. J. 2007, in IAU Symposium, Vol. 242, Astrophysical Masers and their Environments, ed. J. M. Chapman & W. A. Baan, 522–529

Rodríguez-Garza, C. B., Kurtz, S. E., Gómez-Ruiz, A. I., et al. 2017, ApJS, 233, 4

Ruiz-Velasco, A. E., Felli, D., Migenes, V., & Wiggins, B. K. 2016, ApJ, 822, 101

Sarma, A. P. & Momjian, E. 2009, ApJ, 705, L176

Sarma, A. P. & Momjian, E. 2011, ApJ, 730, L5

Sarma, A. P. & Momjian, E. 2020, ApJ, 890, 6

Sarma, A. P., Troland, T. H., & Romney, J. D. 2001, ApJ, 554, L217

Sarma, A. P., Troland, T. H., Romney, J. D., & Huynh, T. H. 2008, ApJ, 674, 295

Shu, F. H., Adams, F. C., & Lizano, S. 1987, ARA&A, 25, 23

Shu, F. H., Galli, D., Lizano, S., & Cai, M. 2006, ApJ, 647, 382

Stepanovs, D., Fendt, C., & Sheikhnezami, S. 2014, ApJ, 796, 29

Stephens, I. W., Yang, H., Li, Z.-Y., et al. 2017, ApJ, 851, 55

Surcis, G., Vlemmings, W. H. T., Curiel, S., et al. 2011a, A&A, 527, A48

Surcis, G., Vlemmings, W. H. T., Dodson, R., & van Langevelde, H. J. 2009, A&A, 506, 757

Surcis, G., Vlemmings, W. H. T., Torres, R. M., van Langevelde, H. J., & Hutawarakorn Kramer, B. 2011b, A&A, 533, A47

Surcis, G., Vlemmings, W. H. T., van Langevelde, H. J., et al. 2014, A&A, 565, L8

Surcis, G., Vlemmings, W. H. T., van Langevelde, H. J., & Hutawarakorn Kramer, B. 2012, A&A, 541, A47

Surcis, G., Vlemmings, W. H. T., van Langevelde, H. J., Hutawarakorn Kramer, B., & Bartkiewicz, A. 2019, A&A, 623, A130

Surcis, G., Vlemmings, W. H. T., van Langevelde, H. J., et al. 2015, A&A, 578, A102

Surcis, G., Vlemmings, W. H. T., van Langevelde, H. J., Hutawarakorn Kramer, B., & Quiroga-Nuñez, L. H. 2013, A&A, 556, A73

Tan, J. C., Kong, S., Butler, M. J., Caselli, P., & Fontani, F. 2013, ApJ, 779, 96

Tassis, K., Willacy, K., Yorke, H. W., & Turner, N. J. 2014, MNRAS, 445, L56

Tazaki, R., Lazarian, A., & Nomura, H. 2017, ApJ, 839, 56

Teyssier, R. & Commerçon, B. 2019, Frontiers in Astronomy and Space Sciences, 6, 51

Torrelles, J. M., Gómez, J. F., Rodríguez, L. F., et al. 1997, ApJ, 489, 744

Torrelles, J. M., Patel, N. A., Anglada, G., et al. 2003, ApJ, 598, L115

Troland, T. H. & Heiles, C. 1982, ApJ, 252, 179

Vaillancourt, J. E., Dowell, C. D., Hildebrand , R. H., et al. 2008, ApJ, 679, L25

Vázquez-Semadeni, E., Banerjee, R., Gómez, G. C., et al. 2011, MNRAS, 414, 2511

Vázquez-Semadeni, E., Kim, J., Shadmehri, M., & Ballesteros-Paredes, J. 2005, ApJ, 618, 344

Vlemmings, W., Diamond, P. J., & van Langevelde, H. J. 2001, A&A, 375, L1

Vlemmings, W. H. T. 2007, in IAU Symposium, Vol. 242, Astrophysical Masers and their Environments, ed. J. M. Chapman & W. A. Baan, 37–46

Vlemmings, W. H. T. 2008, A&A, 484, 773

Vlemmings, W. H. T., Diamond, P. J., van Langevelde, H. J., & Torrelles, J. M. 2006, A&A, 448, 597

Vlemmings, W. H. T., Humphreys, E. M. L., & Franco-Hernández, R. 2011a, ApJ, 728, 149

Vlemmings, W. H. T., Lankhaar, B., Cazzoletti, P., et al. 2019, A&A, 624, L7

Vlemmings, W. H. T., Surcis, G., Torstensson, K. J. E., & van Langevelde, H. J. 2010, MNRAS, 404, 134

Vlemmings, W. H. T., Torres, R. M., & Dodson, R. 2011b, A&A, 529, A95

Voronkov, M. A., Brooks, K. J., Sobolev, A. M., et al. 2006, MNRAS, 373, 411

Wang, K., Zhang, Q., Testi, L., et al. 2014, MNRAS, 439, 3275

Watson, W. 2008, in Cosmic Agitator: Magnetic Fields in the Galaxy, 21

Weaver, H., Williams, D. R. W., Dieter, N. H., & Lum, W. T. 1965, Nature, 208, 29

Weingartner, J. C. & Draine, B. T. 2003, ApJ, 589, 289

Weinreb, S., Meeks, M. L., & Carter, J. C. 1965, Nature, 208, 440

Western, L. R. & Watson, W. D. 1984, ApJ, 285, 158

Wiebe, D. S. & Watson, W. D. 1998, ApJ, 503, L71

Wiesemeyer, H., Thum, C., & Walmsley, C. M. 2004, A&A, 428, 479

Wurster, J. & Li, Z.-Y. 2018, Frontiers in Astronomy and Space Sciences, 5, 39

Zhang, Q., Qiu, K., Girart, J. M., et al. 2014, ApJ, 792, 116

Acknowledgements

First of all, I want to deeply thank my supervisor, Prof. Wouter Vlemmings: it has been an extremely valuable and enriching experience being your student and learning from you about masers and magnetic fields. I am really grateful for all your insightful comments, your prompt help and precise feedback.

A great thank you goes to Dr. Gabriele Surcis for providing me with precious comments and suggestions. Many thanks also to Dr. Magnus Persson, Dr. Daniel Tafoya and all my collaborators for the interesting scientific discussions and the valuable help. A big thank you to Dr. Robert Cumming for the engaging exchanges about science communication and to Prof. Alessandro Romeo for the competent advice on pedagogy and teaching. I also want to express my gratitude to all the people at Onsala Space Observatory and at the Department of Space, Earth and Environment: it has been a pleasure to spend these years with you!

I'm really lucky to have met such a heart-warming friend like Maryam: you are the best office-mate ever and it has been amazing to share these years with you. Thank you for all the funny times we spent together and for your unwavering frienship! A special thank you to Sandra: we are all "emigrantes" but I felt a bit more at home since I have met you. A big thank you also to all my PhD and post-doc fellows, present and past, for all the pleasant times we spent together. And in particular I want to thank Flora, Periklis, Grzegorz, Niko, Mitra, Joakim, Jean-Baptiste, Iskra, Jonas, Andri, Boy, Sara, Hannah, Judit, Juan, Chia-Jung, Jan and Sabine.

A unique thank you to Piero and Leonida for cheering me up and making every day a special day. Finally, I want to thank all my family and my friends for their love and support during these years. We couldn't see each other as often as we wished, but all the moments we spent together were memorable and refreshing. I can't wait to hug you again, hopefully soon. Amalia, Andrea, Glenda, Melinda, Manuela, Luca... amici miei tutti, non vedo l'ora di farmi un tuffo al mare con voi la prossima estate, magari con una piadina e due cappelletti, voi sapete dove... preparatevi! :)

Daria

Onsala, September 2020